ARTICLES
PUBLISHED ONLINE: 29 JUNE 2015 | DOI: 10.1038/NPHOTON.2015.110

nature photonics

Harnessing high-dimensional hyperentanglement through a biphoton frequency comb

Zhenda Xie[1,2]*, Tian Zhong[3], Sajan Shrestha[2], XinAn Xu[2], Junlin Liang[2], Yan-Xiao Gong[4], Joshua C. Bienfang[5], Alessandro Restelli[5], Jeffrey H. Shapiro[3], Franco N. C. Wong[3] and Chee Wei Wong[1,2]*

Quantum entanglement is a fundamental resource for secure information processing and communications, and hyperentanglement or high-dimensional entanglement has been separately proposed for its high data capacity and error resilience. The continuous-variable nature of the energy–time entanglement makes it an ideal candidate for efficient high-dimensional coding with minimal limitations. Here, we demonstrate the first simultaneous high-dimensional hyperentanglement using a biphoton frequency comb to harness the full potential in both the energy and time domain. Long-postulated Hong–Ou–Mandel quantum revival is exhibited, with up to 19 time-bins and 96.5% visibilities. We further witness the high-dimensional energy–time entanglement through Franson revivals, observed periodically at integer time-bins, with 97.8% visibility. This qudit state is observed to simultaneously violate the generalized Bell inequality by up to 10.95 standard deviations while observing recurrent Clauser–Horne–Shimony–Holt *S*-parameters up to 2.76. Our biphoton frequency comb provides a platform for photon-efficient quantum communications towards the ultimate channel capacity through energy–time–polarization high-dimensional encoding.

Increasing the dimensionality of quantum entanglement is a key enabler for high-capacity quantum communications and key distribution[1,2], quantum computation[3] and information processing[4,5], imaging[6] and enhanced quantum phase measurement[7,8]. A large Hilbert space can be achieved through entanglement in more than one degree of freedom (known as hyperentanglement[2,7,9]), where each degree of freedom can also be expanded to more than two dimensions (known as high-dimensional entanglement). The high-dimensional entanglement can be prepared in several physical attributes, for example, in orbital angular momentum[1,10–12] and other spatial modes[13–15]. The drawback of these high-dimensional spatial states is complicated beam-shaping for entanglement generation and detection, which reduces the brightness of the sources as the dimension scales up and complicates their use in optical-fibre-based communications systems. In contrast, the continuous-variable energy–time entanglement[16–22] is intrinsically suitable for high-dimensional coding and, if successful, can potentially be generated and communicated via the telecommunication network. However, most studies focus on time-bin entanglement, which is discrete-variable entanglement with a typical dimensionality of two[23–25]. Difficulties in pump-pulse shaping and phase control limit the dimensionality of the time-bin entanglement[26], and high-dimensional time-bin entanglement has not been fully characterized because of the overwhelmingly complicated analysing interferometers. On the other hand, a biphoton state with a comb-like spectrum could potentially serve for high-dimensional entanglement generation and take full advantage of the continuous-variable energy–time subspace. Based on this state, promising applications have been proposed for quantum computing, secure wavelength-division multiplexing and dense quantum key distribution[3,27,28]. A phase-coherent biphoton frequency comb (BFC) is also known for its mode-locked behaviour in its second-order correlation. Unlike classical frequency combs, where mode-locking directly relies on phase coherence over individual comb lines, the mode-locked behaviour of a BFC is the representation of the phase coherence of a biphoton wavepacket over comb-line pairs and results in periodic recurrent correlation at different time-bins[29,30]. This time correlation feature can be characterized through quantum interference when passing the BFC through an unbalanced Hong–Ou–Mandel (HOM)-type interferometer[31]. A surprising revival of the correlation dips can be observed at time-bins with half the period of the BFC revival time. However, because of the limited type-I collinear spontaneous parametric downconversion (SPDC) configuration in previous studies[29], post-selection was necessary for BFC generation where the signal and idler photons are indistinguishable, limiting the maximum two-photon interference to 50%.

Here, we achieve high-dimensional hyperentanglement through a BFC. The high-dimensional hyperentanglement of the BFC is fully characterized by four observations. First, the state is prepared at telecommunications wavelengths, without the need for post-selection, by using a type-II high-efficiency periodically-poled $KTiOPO_4$ (ppKTP) waveguide together with a fibre Fabry–Pérot cavity (FFPC). Because of the type-II phase matching, signal and idler photons can be separated efficiently by a polarizing beamsplitter (PBS), allowing deterministic BFC generation (as first proposed theoretically by one of the authors of ref. 29) to be observed experimentally for the first time. Revival dips with ≈96.5% visibility from two-photon interference in a HOM-type interferometer are observed recurrently, also for the first time, revealing correlation

---

[1]Mesoscopic Optics and Quantum Electronics Laboratory, University of California, Los Angeles, California 90095, USA. [2]Optical Nanostructures Laboratory, Columbia University, New York, New York 10027, USA. [3]Research Laboratory of Electronics, Massachusetts Institute of Technology, Cambridge, Massachusetts 02139, USA. [4]Department of Physics, Southeast University, Nanjing 211189, People's Republic of China. [5]Joint Quantum Institute, University of Maryland and National Institute of Standards and Technology, Gaithersburg, Maryland 20899, USA. *e-mail: zhenda@seas.ucla.edu; cheewei.wong@ucla.edu

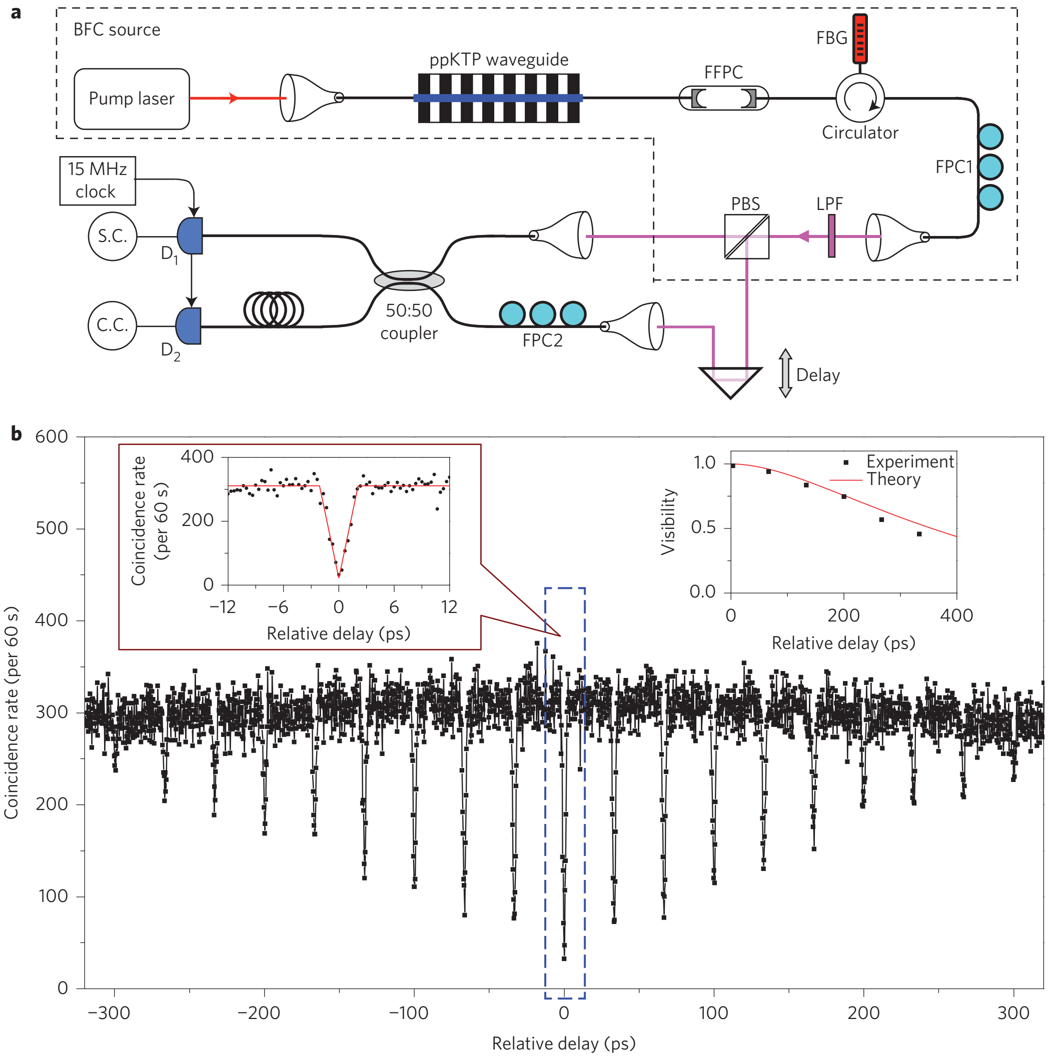

Figure 1 | Generation and quantum revival observations of the high-dimensional biphoton frequency comb. a, Illustrative experimental scheme. FFPC, fibre Fabry–Pérot cavity; FBG, fibre Bragg grating; FPC, fibre polarization controller; LPF, long-pass filter; PBS, polarizing beamsplitter; P, polarizer; S.C., single counts; C.C., coincidence counts. **b**, Coincidence counting rate as a function of relative delay, ΔT, between the two arms of the HOM interferometer. The HOM revival is observed in the two-photon interference, with dips at 19 time-bins in this case. The visibility change across the different relative delays arises from the single FFPC bandwidth, $\Delta\omega$. The red solid line is the theoretical prediction from the phase-matching bandwidth. Left inset: zoom-in coincidence around zero relative delay between the two arms. The dip width was fit to be 3.86 ± 0.30 ps, which matches well with the 245 GHz phase-matching bandwidth. The measured visibility of the dip is observed at 87.2 ± 1.5, or 96.5% after subtracting the accidental coincidence counts. Right inset: measured bin visibility versus HOM delay, compared with theoretical predictions (Supplementary Section I).

features in the time-bins of the BFC. Second-order frequency correlation and anticorrelation, scanned across the full span of the frequency-bins by narrowband filter pairs, show the good fidelity of the frequency-bin entangled state. Finally, we confirm the generation of high-dimensional energy–time entanglement using a Franson interferometer, which can be regarded as a generalized Bell inequality test. For the first time, Franson interference fringes are observed to revive periodically at different time-bin intervals with visibilities up to 97.8%. Based on these three measurements, we encode extra qubits in the BFC photon pairs by mixing them on a 50:50 fibre beamsplitter (FBS). We witness the hyperentanglement by simultaneous polarization and Franson interferometer analysis, demonstrating a generalized Bell inequality in two polarization and four time-bin subspaces up to 10.95 and 8.34 standard deviations (s.d.) respectively. The Clauser–Horne–Shimony–Holt (CHSH) *S*-parameters are determined for the polarization basis across the different time-bins with a maximum up to 2.76.

Figure 1a presents the experimental scheme. The SPDC entangled photon pairs are generated by a high-efficiency type-II ppKTP waveguide, described in detail in ref. 32. The frequency-degenerate SPDC phase matching is designed for a 1,316 nm output with a bandwidth of ≈245 GHz. The type-II BFC is generated by passing the SPDC photons through a FFPC (Micron Optics; note that the identification of any commercial product or trade name does not imply endorsement or recommendation by the National Institute of Standards and Technology), with the signal and idler photons in orthogonal polarizations (*H*, horizontal; *V*, vertical). A BFC state is expressed as

$$|\psi\rangle = \sum_{m=-N}^{N} \int d\Omega f(\Omega - m\Delta\Omega)\hat{a}_H^{\dagger}(\omega_p/2 + \Omega)\hat{a}_V^{\dagger}(\omega_p/2 - \Omega)|0\rangle \qquad (1)$$

where $\Delta\Omega$ is the spacing between the frequency bins (that is, the free spectral range of the FFPC in rad s^{-1}, Ω is the detuning of the SPDC

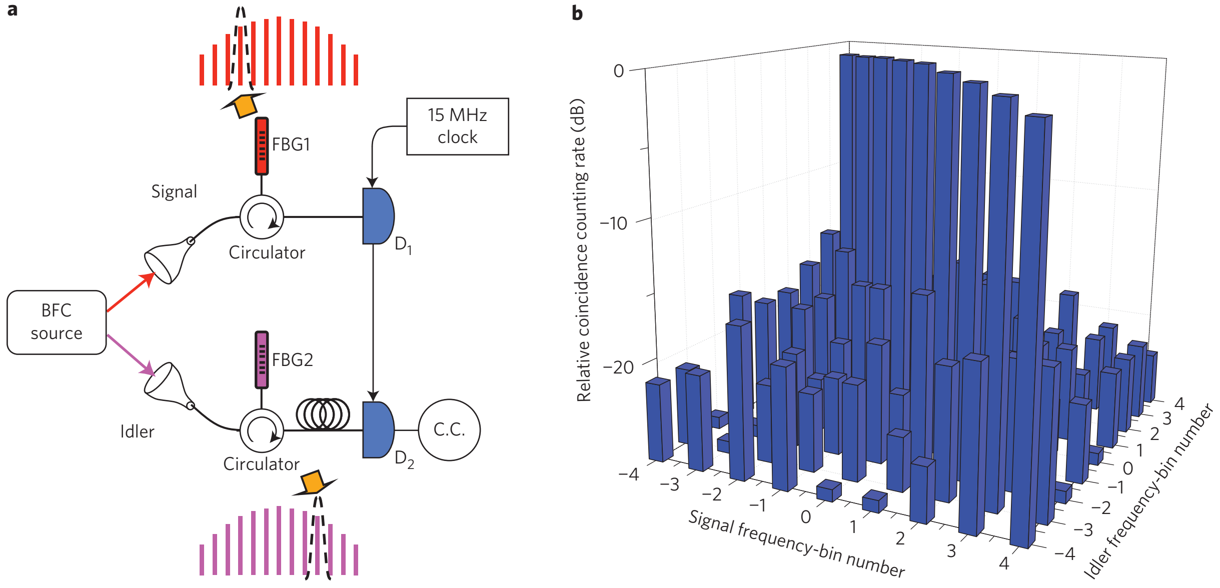

Figure 2 | Quantum frequency correlation measurement of the biphoton frequency comb. a, Experimental schematic for the frequency correlation measurement. Signal and idler photons are sent to two narrowband filters for the frequency bin correlation measurement with coincidence counting. Each filter consists of a FBG and a circulator. The FBGs have a matched FWHM bandwidth of 100 pm and are thermally tuned for scans from the –4th to +4th frequency bins from the centre. **b**, Measured frequency correlation of the BFC. The relative coincidence counting rate is recorded while the signal and idler filters are set at different frequency-bin numbers.

biphotons from their central frequency, and the state's spectral amplitude $f(\Omega - m\Delta\Omega)$ is the single frequency-bin profile, defined by the Lorentzian-shape transmission of the FFPC with a full-width at half-maximum (FWHM) of $2\Delta\omega$, and

$$f(\Omega) = \frac{1}{[(\Delta\omega)^2 + \Omega^2]} \tag{2}$$

The signal and idler photons are separated with 100% probability by a polarizing beamsplitter or, in other words, the BFC is thus prepared without post-selection. The temporal wavefunction of the BFC can be written as

$$|\psi_t\rangle = \int \mathrm{d}\tau \exp(-\Delta\omega|\tau|)\frac{\sin[(2N+1)\Delta\Omega\tau/2]}{\sin(\Delta\Omega\tau/2)}\hat{a}_H^\dagger(t)\hat{a}_V^\dagger(t+\tau)|0\rangle \tag{3}$$

where the exponential decay is slowly varying because of small $\Delta\omega$ and thus the temporal behaviour of the BFC is mainly determined by the term $(\sin[(2N+1)\Delta\Omega\tau/2]/\sin(\Delta\Omega\tau/2))$, with a repetition time of $T = 2\pi/\Delta\Omega$.

The FFPC has a free spectral range (FSR) and bandwidth of 15.15 GHz and 1.36 GHz, respectively. The repetition period T of the BFC is ≈66.2 ps. The FFPC is mounted onto a thermoelectric cooling sub-assembly with minimized stress to eliminate polarization birefringence and with ≈1 mK high-performance temperature control. From our measurements, there is no observable polarization birefringence in the FFPC, so the signal and idler photons have the same spectrum after they pass through the cavity. Due to the type-II configuration, there is no probability that both photons propagate in the same arm of the HOM interferometer; this configuration yields a potential maximum of 100% visibility of the two-photon interference.

The pump is a Fabry–Pérot laser diode that is stabilized with self-injection-locking through double-pass first-order-diffraction feedback using an external grating (for details see Supplementary Section IV and Methods). It is passively stabilized with modest low-noise current and temperature control for single-longitudinal-mode lasing at 658 nm, with a stability of less than 2 MHz within 200 s (measured with the Franson interference experiment; Supplementary Section IV). We first match the FFPC wavelength with the pump via temperature tuning and second harmonic generation (SHG) from a frequency-stabilized distributed feedback (DFB) reference laser at 1,316 nm. The SHG is monitored with a wavemeter (WS-7, HighFinesse) to 60 MHz accuracy, allowing the tuning of the laser diode current and first-order-feedback diffraction angle to match the FFPC for BFC generation. The BFC spectrum is further cleaned by a fibre Bragg grating (FBG) with a circulator and a free-space long-pass filter that blocks residual pump light. The FBG is chosen to have a bandwidth of 346 GHz, larger than the 245 GHz phase-matching bandwidth, and is simultaneously temperature-controlled to match the central wavelength of the SPDC. A polarizing beamsplitter separates the orthogonally polarized signal and idler photons.

We first characterize the mode-locked behaviour using a HOM interferometer. The signal and idler photons are sent through different arms of the interferometer. A fibre polarization controller in the interferometer's lower arm controls the idler photon polarization, so that the two photons have the same polarization at the FBS. An optical delay line consisting of a prism and a motorized long-travel linear stage (DDS220, Thorlabs) is used to change the relative timing delay between the two arms of the HOM interferometer. The position-dependent insertion loss of the optical delay line is measured to be less than 0.02 dB throughout its entire travel range of 220 mm. The coincidence measurements are performed with two InGaAs single-photon detectors D_1 (≈20% detection efficiency and 1 ns gate width) and D_2 (≈25% detection efficiency and 3 ns gate width). D_1 is triggered at 15 MHz, and its output signal is used to trigger D_2. As a result, coincidences can be detected directly from the D_2 counting rate if the proper optical delay is applied to compensate for the electronic delay. Taking into account the waveguide-to-fibre coupling and transmission efficiencies of the optical components, the overall signal and idler detection efficiencies are estimated to be $\eta_s = 0.92\%$ and $\eta_i = 1.14\%$, respectively. Figure 1b shows the experimental results obtained by scanning the optical

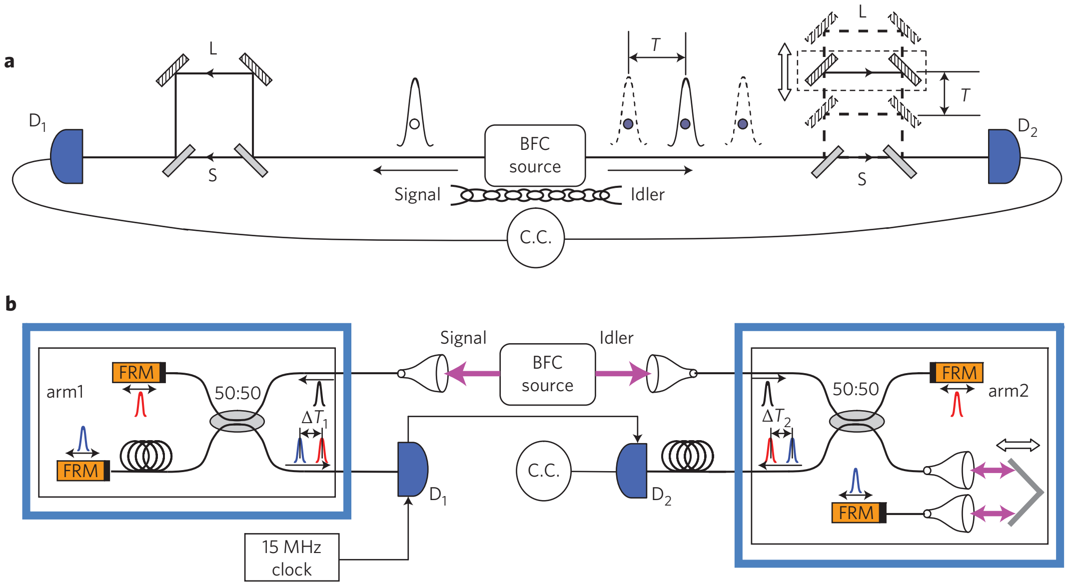

Figure 3 | Franson interference of the high-dimensional biphoton frequency comb. a, Schematic map and concept of Franson interference of the BFC. The BFC is prepared with high-dimensional correlation features of mode-locked behaviour with a repetition period of T. Franson-type interference between the long–long (L–L) and short–short (S–S) events can therefore be observed when $\Delta T = NT$, where N is an integer. **b**, Experimental Franson interference set-up. Faraday mirrors (FRMs) are used to compensate the stress-induced birefringence of the single-mode fibre interferometers. A compact optical delay line was used in the longer path of arm2 to achieve different imbalances ΔT (= $\Delta T_2 - \Delta T_1$). Both arms are double-temperature stabilized, first on the custom aluminium plate mountings and second by the sealed enclosures (light blue thick lines).

delay between the two arms of the HOM interferometer from −320 ps to 320 ps, with a pump power of 2 mW. At this power level the generation rate is $\approx 3.3 \times 10^{-3}$ pairs per gate, and multi-pair events can be neglected. We obtain revival dips for the coincidence counting rate R_{12} at the two outputs of the HOM interferometer (single-photon rates are shown in Supplementary Section V). The spacing between the dips is 33.4 ps, which matches half the repetition period of the BFC, and agrees with our theory and numerical modelling (see Supplementary Section I for details). We also note that our earlier analysis[30] involved a movable beamsplitter for both beams (for a T recurrence), but in the present measurement set-up only the idler beam is delayed (for a $T/2$ recurrence), supported by the same type of analysis and physical interpretation. The visibility of the dips decreases exponentially (right inset in Fig. 1b) due to the Lorentzian lineshape spectra of the SPDC individual photons after they pass through the FFPC. A zoom-in of the dip around the zero delay point is shown in the left inset of Fig. 1b. The maximum visibility is measured to be 87.2 ± 1.5, or 96.5% after subtracting the accidental coincidence counts (≈17.3 per 70 s). Its base-to-base width is fitted to be 3.86 ± 0.30 ps, corresponding to a two-photon bandwidth of 259 ± 20 GHz, which agrees with the expected 245 GHz phase-matching bandwidth. More details are provided in Supplementary Section V. Considering the measured bin spacing $\Delta\Omega/2\pi$ of 14.98 GHz, 17 frequency-bins are generated in our measurements within the phase-matching bandwidth, equivalent to ≈4 quantum bits per photon for high-dimensional frequency entanglement.

To test the purity of the high-dimensional frequency-bin entanglement, we further measure the correlation between different frequency-bins for the signal and idler photons. Each pair of frequency-bins is filtered out by a set of narrowband filters for the signal and idler photons. As shown in Fig. 2, each filter is composed of a FBG centred at 1,316 nm with 100 pm FWHM and an optical circulator. Both FBGs are embedded in a custom-built temperature-controlled housing for fine spectral tuning. The coincidence counting rate is recorded while the filters are set at different combinations of the signal–idler frequency-bin basis. The tuning range is bounded by the maximum tuned FBG temperature (currently up to ≈100 °C), and in this case nine frequency-bins can be examined for the signal and idler biphoton. We number these bins #−4 to #4, with #0 indicating the central bin, as shown in Fig. 2b. We see that high coincidence counting rates are measured only when the filters are set at the corresponding positive–negative frequency-bins, according to equation (1). The suppression ratio between the corresponding and non-corresponding counting rate exceeds 13.8 dB for adjacent bins (including ≈2% leakage from the bandpass filters), or 16.6 dB for non-adjacent bins. We note that, through conjugate state projection[20], observation of both the HOM recurrence and frequency correlation supports the entangled nature of the BFC.

To further characterize the energy–time entanglement of the BFC, we built an interferometer to examine Franson interference, as shown schematically in Fig. 3a. The Franson interferometer[16,33] comprises two unbalanced Mach–Zehnder interferometers (for details see Supplementary Methods and Supplementary Section III), with imbalances ΔT_1 and ΔT_2. Usually, Franson interference arises from two indistinguishable two-photon events: both signal and idler photons take the long arm (L–L) and both photons take the short arm (S–S). This interference only happens when $\Delta T \equiv \Delta T_1 - \Delta T_2 = 0$ to within the single photon coherence length, which is 1.81 ps in our case. Because of the high-dimensional frequency entanglement, however, Franson interference can be observed at different time revivals. As discussed before, the BFC features a mode-locked revival in temporal correlation, with a repetition period of T. Such Franson interference revival can therefore be observed for integer temporal delays $\Delta T = NT$, where N is an integer (including 0). Detailed theory and modelling are provided in Supplementary Section II for the revival of the Franson interference, and the experimental set-up is shown in Fig. 3b. The signal and idler photons are sent to two fibre-based interferometers (arm1 and arm2) with imbalances ΔT_1 and ΔT_2, respectively. Details on the pump laser and interferometer set-up stabilisation are described in Supplementary Sections III and IV and in the Methods. Each arm includes double-pass temperature-stabilized

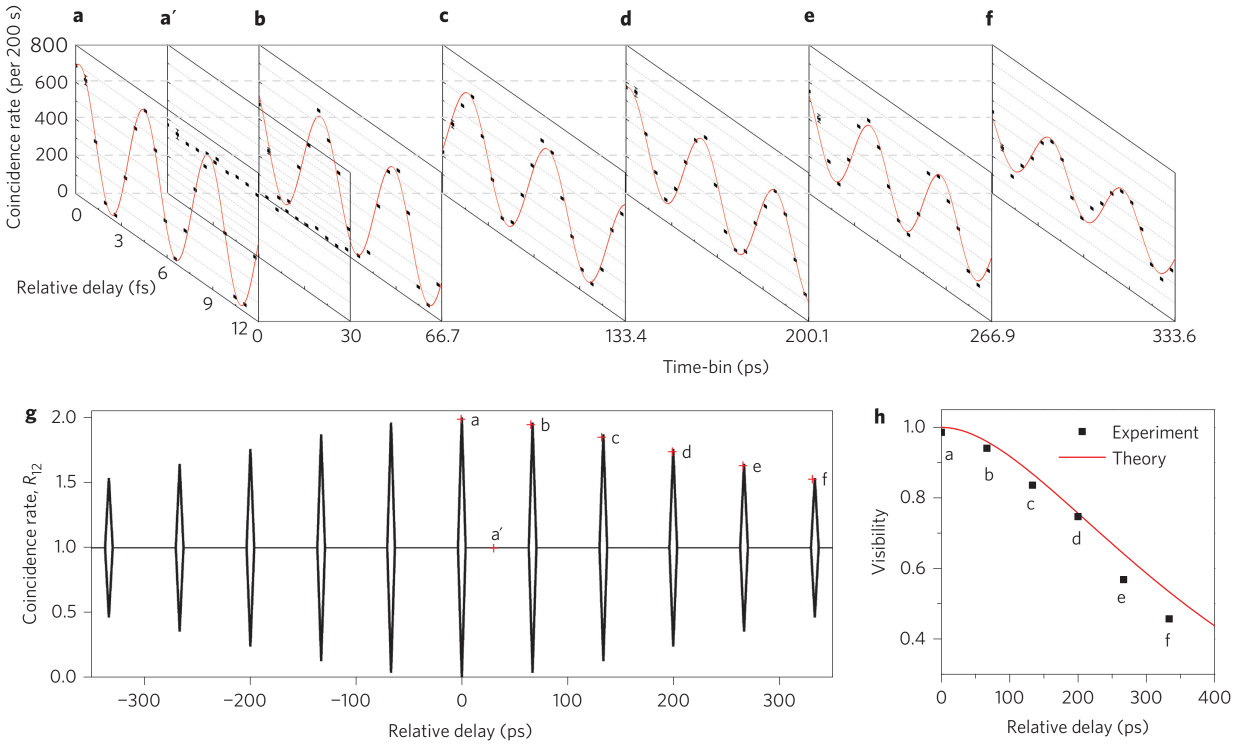

Figure 4 | Measured Franson interference around different relative delays of arm2. a–f, Franson interferences at time-bins #0 ($\Delta T = 0$), #1 ($\Delta T = 66.7$ ps), #2 ($\Delta T = 133.4$ ps), #3 ($\Delta T = 200.1$ ps), #4 ($\Delta T = 266.9$ ps) and #5 ($\Delta T = 333.6$ ps), respectively. Also included in **a′** is the interference measured away from the above time-bins at $\Delta T = 30$ ps, with no observable interference fringes. The data points in each panel (of the different relative Franson delays) include the measured error bars across each data set, arising from Poisson statistics, experimental drift and measurement noise. The error bars from repeated coincidence measurements are much smaller than the observed coincidence rates in our measurement and set-up. In each panel, the red line denotes the numerical modelling of the Franson interference on the high-dimensional quantum state. **g**, Theoretical fringe envelope of Franson interference for the high-dimensional biphoton frequency comb, with superimposed experimental observations. The marked labels (**a–f**,**a′**) correspond to the actual delay points from which the above measurements were taken. **h**, Witnessed visibility of high-dimensional Franson interference fringes as a function of ΔT. The experimental (and theoretical) witnessed visibilities for the *k*th-order peaks are 97.8 (100), 93.3 (96.0), 83.0 (86.8), 74.1 (75.6), 59.0 (64.0) and 45.4% (53.3%), respectively.

Michelson interferometers, and two of the output ports of the fibre 50:50 beamsplitter are spliced onto two Faraday mirrors, with single photons being collected from the reflection. They therefore effectively work as a Mach–Zehnder interferometer, and the polarization instability inside the fibres is self-compensated accurately. Following the general requirement for Franson interference, the ΔT_1 and ΔT_2 time differences (5 ns in our set-up) are tuned to be much larger than the single-photon coherence time and the timing jitter of the single-photon detectors. The relative timing between the single-photon detection gates is programmed such that events are only recorded for the L–L and S–S events. Both arms are mounted on aluminium housings with ≈1 mK temperature control accuracy. Enclosures are further used to seal the interferometers with additional temperature control for isolating mechanical and thermal shocks. To detect the Franson interference at different temporal revivals, we include a free-space delay line on arm2, which gives us the capability to study the Franson interference with possible detuning ΔT up to 360 ps, bounded by the free-space delay line travel and for up to six positive-delay time-bins.

We are interested here in the regime of $\Delta T \geq 0$, because of the symmetry of the signal and idler. In particular, this allows us to examine the interference visibility over a larger time frame, for the same stage travel range. With ΔT_2 fixed at each point, the phase-sensitive interference is achieved by fine control of the arm1 temperature, which tunes ΔT_1. As shown in Fig. 4, the revival of Franson interference is only observed exactly at the periodic time-bins $\Delta T = NT$, whereas no interference is observed for other ΔT values between these bins. The period of the revival time bins is 66.7 ps, which corresponds exactly to the round-trip time of the FFPC ($2\pi/\Delta\Omega$). The visibilities of the interference fringes are measured to be 94.2, 89.3, 79.7, 71.1, 51.0 and 43.6%, or, after subtracting the accidental coincidence counts, 97.8, 93.3, 83.0, 74.1, 59.0 and 45.4%, respectively. The visibility decreases because of the non-zero linewidth of each frequency bin and is captured in our theory (Supplementary Section II). We understand this as a generalized Bell inequality violation for a high-dimensional state at four time-bins from the centre. We only measured for $\Delta T \geq 0$, but could expect the violation of the generalized Bell inequality at the other three inverse symmetric time bins of ΔT at −66.7 ps, −133.4 ps and −200.1 ps, based on symmetry with the three positive time-bins observed.

Figure 5 shows the high-dimensional hyperentanglement by mixing the signal and idler photons on a 50:50 FBS (for details see Supplementary Section VI). In the experiment, hyperentanglement is generated based on the HOM-interference set-up fixed at the central dip, but with polarization adjusted so that the signal and idler photons are orthogonally polarized at the FBS for hyperentanglement generation. Two polarizers P_1 and P_2 are used for the polarization analysis, which is cascaded with the Franson interferometer for the energy–time entanglement measurement at the same time. One set of half and quarter waveplates are placed before each polarizer to compensate the polarization change in the fibre after the FBS. An additional thick multi-order full waveplate is used in the lower arm, which can be twisted along its

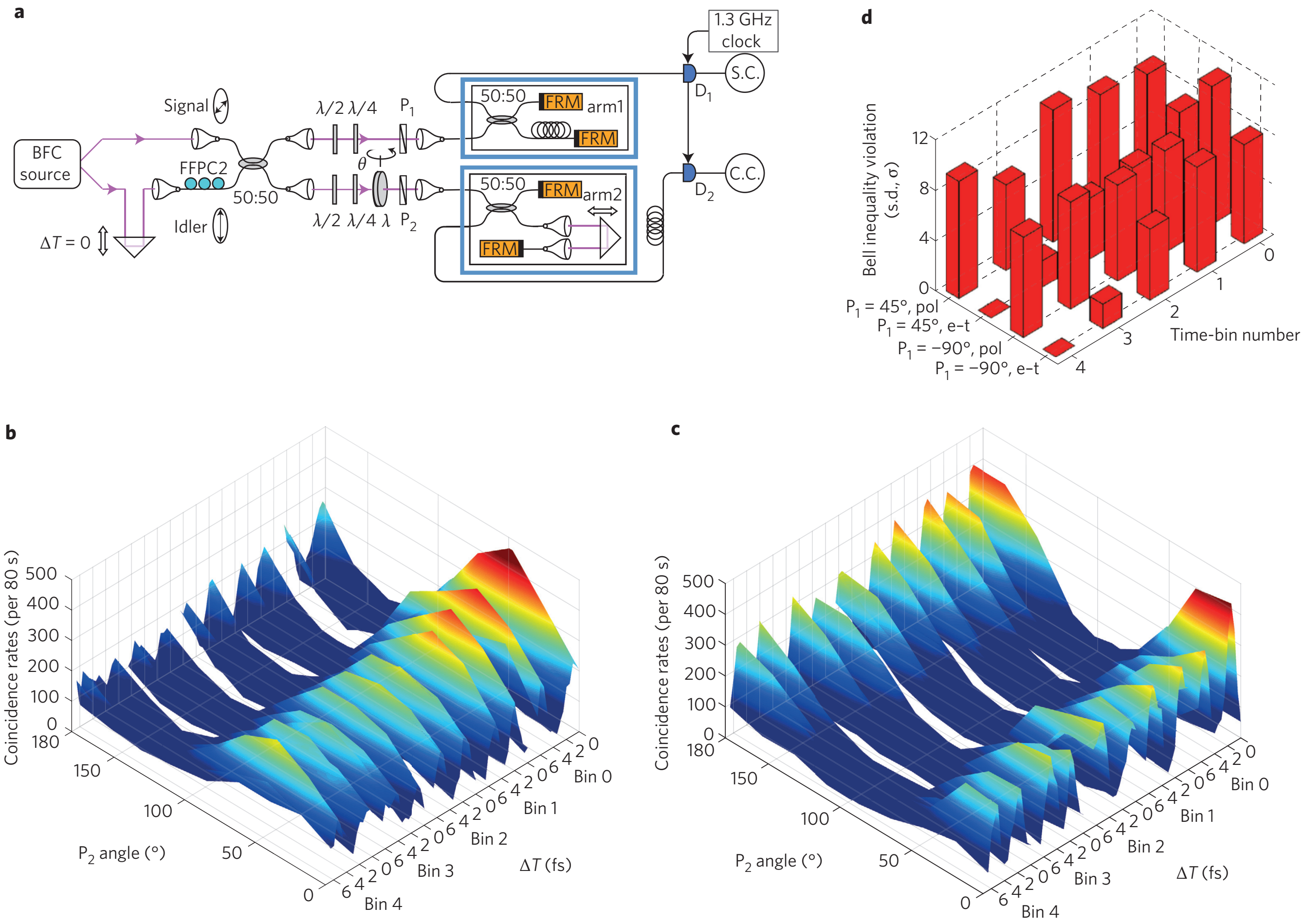

Figure 5 | High-dimensional hyperentanglement on polarization and energy–time basis. a, Set-up for the high-dimensional two degree-of-freedom entanglement measurement. The state is generated by mixing the signal and idler photons at the 50:50 fibre beamsplitter with orthogonal polarizations. Perfect temporal overlap between signal and idler photons is ensured by the HOM interference, as already discussed. High-dimensional hyperentanglement is measured with polarization analysis using polarizers P_1 and P_2, cascaded with a Franson interferometer. $\lambda/2$, half waveplate; $\lambda/4$, quarter waveplate; λ, multi-order full waveplate. **b**,**c**, Measured two-photon interference fringes when P_1 is set at 45 and 90 degrees, respectively. The period variance of the fringe on the temporal domain arises because of a slow pump laser drift. **d**, Measured Bell inequality violation at different time-bins and P_1 angles. pol, polarization basis; e-t, energy–time basis.

fast axis (fixed in the horizontal plane) to change the phase delay between the horizontally and vertically polarized light. Therefore, we successfully generated the following high-dimensional hyperentangled state when a coincidence is measured:

$$|\psi'\rangle = \sum_{m=-N}^{N} \int \mathrm{d}\Omega f(\Omega - m\Delta\Omega) \times (|H, \omega_p/2 + \Omega\rangle_1 |V, \omega_p/2 - \Omega\rangle_2 + |V, \omega_p/2 + \Omega\rangle_1 |H, \omega_p/2 - \Omega\rangle_2) \tag{4}$$

Such hyperentanglement is tested using coincidence measurement by scanning P_2 and the Franson interferometer while P1 is set at 45° or 90° and ΔT is fixed at time-bins #0 to #5. A 1.3 GHz self-differencing InGaAs single-photon detector[34,35] is used as D_1 to maximize the gated detection rate. As shown in Fig. 5b,c, clear interference fringes were obtained over both the polarization and energy–time basis, with visibilities up to 96.7 and 95.9%, respectively, after dark count subtraction of a 0.44 s^{-1} rate. Analysed within the two polarization and four time-bin subspaces, this corresponds to Bell violation up to 10.95 and 8.34 s.d., respectively. The CHSH S-parameter is observed for the polarization basis up to $S = 2.76$; details on the photon statistics are presented in Fig. 5d and listed in Supplementary Section VII, Table 1.

In summary, we have demonstrated a high-dimensional hyperentanglement of polarization and energy–time subspaces using a BFC. Based on continuous-variable energy–time entanglement, unlimited qubits can be coded on the BFC by increasing the number of comb line pairs with a plane wave pump. Here, we show an example of bright BFC generation with 5 qubits per photon, from a type-II SPDC process in a ppKTP waveguide without post-selection. Nineteen HOM dip recurrences with a maximum visibility of 96.5% are observed in a stabilized interferometer. High-dimensional energy–time entanglement is proven by Franson interference, which can be considered as a generalized Bell inequality test. Revival of the Franson interference has been witnessed at periodic time-bins, where the time-bin separation is the cavity round-trip time, that is, the revival time of the BFC. The interference visibility was measured up to 97.8%. The generalized Bell inequality was violated in four out of six measured time-bins, or seven time-bins in total considering the symmetry. High-dimensional hyperentanglement was further generated and characterized with high fidelity in both polarization and energy–time subspaces, with Bell inequality violations up to 10.95 and 8.34 s.d. respectively, with measured polarization CHSH S-parameters up to 2.76. It should be noted that the generation rate of the entangled biphoton frequency comb from our high-performance ppKTP waveguide exceeds 72.2 pairs s^{-1} MHz^{-1} mW^{-1}, taking into account all detection losses and the 1.5% duty cycle for the detection time, which is higher than that of cavity-enhanced SPDC using bulk crystals. If the propagation loss of the ppKTP waveguide can be further reduced, the waveguide can be located inside an optical cavity and the brightness of the BFC further enhanced. Such a bright high-dimensional hyperentangled BFC can encode multiple qubits onto a single photon pair without losing the high photon flux and thus further increase the photon efficiency, with applications in dense quantum information processing and secure quantum key distribution channels.

Methods

Methods and any associated references are available in the online version of the paper.

Received 23 December 2014; accepted 20 May 2015;

References

1. Dada, A. C., Leach, J., Buller, G. S., Padgett, M. J. & Andersson, E. Experimental high-dimensional two-photon entanglement and violations of generalized Bell inequalities. *Nature Phys.* **7,** 677–680 (2011).
2. Barreiro, J. T., Wei, T. C. & Kwiat, P. G. Beating the channel capacity of linear photonic superdense coding. *Nature Phys.* **4,** 282–286 (2008).
3. Menicucci, N. C., Flammia, S. T. & Pfister, O. One-way quantum computing in the optical frequency comb. *Phys. Rev. Lett.* **101,** 130501 (2008).
4. Krenn, M. *et al.* Generation and confirmation of a (100 × 100)-dimensional entangled quantum system. *Proc. Natl Acad. Sci. USA* **111,** 6243–6247 (2014).
5. Strobel, H. *et al.* Fisher information and entanglement of non-Gaussian spin states. *Science* **345,** 424–427 (2014).
6. Howland, G. A. & Howell, J. C. Efficient high-dimensional entanglement imaging with a compressive-sensing double-pixel camera. *Phys. Rev. X* **3,** 011013 (2013).
7. Bao, W.-B. *et al.* Experimental demonstration of a hyper-entangled ten-qubit Schrödinger cat state. *Nature Phys.* **6,** 331–335 (2010).
8. Sun, F. W. *et al.* Experimental demonstration of phase measurement precision beating standard quantum limit by projection measurement. *Europhys. Lett.* **82,** 24001 (2008).
9. Badziag, P., Brukner, C., Laskowski, W., Pterek, T. & Zukowski, M. Experimentally friendly geometrical criteria for entanglement. *Phys. Rev. Lett.* **100,** 140403 (2008).
10. Fickler, R. *et al.* Quantum entanglement of high angular momenta. *Science* **338,** 640–643 (2012).
11. Fickler, R. *et al.* Interface between path and orbital angular momentum entanglement for high-dimensional photonic quantum information. *Nature Commun.* **5,** 4502 (2014).
12. Leach, J. *et al.* Quantum correlations in optical angle–orbital angular momentum variables. *Science* **329,** 662–665 (2010).
13. Peruzzo, A. *et al.* Quantum walks of correlated photons. *Science* **329,** 1500–1503 (2010).
14. Edgar, M. P. *et al.* Imaging high-dimensional spatial entanglement with a camera. *Nature Commun.* **3,** 984 (2012).
15. Dixon, P. B., Howland, G. A., Schneeloch, J. & Howell, J. C. Quantum mutual information capacity for high-dimensional entangled states. *Phys. Rev. Lett.* **108,** 143603 (2012).
16. Franson, J. D. Bell inequality for position and time. *Phys. Rev. Lett.* **62,** 2205–2208 (1989).
17. Shalm, L. K. *et al.* Three-photon energy–time entanglement. *Nature Phys.* **9,** 19–22 (2013).
18. Cuevas, A. *et al.* Long-distance distribution of genuine energy–time entanglement. *Nature Commun.* **4,** 2871 (2013).
19. Thew, R. T., Acin, A., Zbinden, H. & Gisin, N. Bell-type test of energy–time entangled qutrits. *Phys. Rev. Lett.* **93,** 010503 (2004).
20. Lloyd, S., Shapiro, J. H. & Wong, F. N. C. Quantum magic bullets by means of entanglement. *J. Opt. Soc. Am. B* **19,** 312–318 (2002).
21. Ali-Khan, I., Broadbent, C. J. & Howell, J. C. Large-alphabet quantum key distribution using energy–time entangled bipartite states. *Phys. Rev. Lett.* **98,** 060503 (2007).
22. Zhong, T. *et al.* Photon-efficient quantum key distribution using time–energy entanglement with high-dimensional encoding. *New J. Phys.* **17,** 022002 (2015).
23. Takeda, S., Mizuta, T., Fuwa, M., van Loock, P. & Furusawa, A. Deterministic quantum teleportation of photonic quantum bits by a hybrid technique. *Nature* **500,** 315–318 (2013).
24. Jayakumar, H. *et al.* Time-bin entangled photons from a quantum dot. *Nature Commun.* **5,** 4251 (2014).
25. Marcikic, I. *et al.* Time-bin entangled qubits for quantum communication created by femtosecond pulses. *Phys. Rev. A* **66,** 062308 (2002).
26. De Riedmatten, H. *et al.* Tailoring photonic entanglement in high-dimensional Hilbert spaces. *Phys. Rev. A* **69,** 050304(R) (2004).
27. Roslund, J., de Araújo, R. M., Jiang, S., Fabre, C. & Treps, N. Wavelength-multiplexed quantum networks with ultrafast frequency combs. *Nature Photon.* **8,** 109–112 (2014).
28. Pinel, O. *et al.* Generation and characterization of multimode quantum frequency combs. *Phys. Rev. Lett.* **108,** 083601 (2012).
29. Lu, Y. J., Campbell, R. L. & Ou, Z. Y. Mode-locked two-photon states. *Phys. Rev. Lett.* **91,** 163602 (2003).
30. Shapiro, J. H. Coincidence dips and revivals from a Type-II optical parametric amplifier. *Technical Digest of Topical Conference on Nonlinear Optics*, paper FC7-1, Maui, HI, 2002.
31. Hong, C. K., Ou, Z. Y. & Mandel, L. Measurement of subpicosecond time intervals between two photons by interference. *Phys. Rev. Lett.* **59,** 2044–2046 (1987).
32. Zhong, T., Wong, F. N. C., Roberts, T. D. & Battle, P. High performance photon-pair source based on a fiber-coupled periodically poled $KTiOPO_4$ waveguide. *Opt. Express* **17,** 12019–12030 (2009).
33. Gisin, N. & Thew, R. Quantum communication. *Nature Photon.* **1,** 165–171 (2007).
34. Restelli, A. & Bienfang, J. C. Avalanche discrimination and high-speed counting in periodically gated single-photon avalanche diodes. *Proc. SPIE.* **8375,** 83750Z (2012).
35. Yuan, Z. L., Kardynal, B. E., Sharpe, A. W. & Shields, A. J. High speed single photon detection in the near infrared. *Appl. Phys. Lett.* **91,** 041114 (2007).

Acknowledgements

The authors thank T. Pittman, J. Franson and D. Fields for assistance, and A. Kumar Vinod, Y. Li, J. Poekert, M. Itzler, P. Li, D.R. Englund and X. Hu for discussions. This work is supported by the InPho programme of the Defense Advanced Research Projects Agency (DARPA) under contract no. W911NF-10-1-0416. Y.X.G. is supported by the National Natural Science Foundations of China (grant no. 11474050).

Author contributions

Z.X., T.Z., S.S., X.X. and J.L. performed the measurements. J.C.B. and A.R. developed the 1.3 GHz detectors. T.Z., Y.X.G., F.N.C.W. and J.H.S. provided the theory and samples. All authors helped with manuscript preparation.

Additional information

Supplementary information is available in the online version of the paper. Reprints and permissions information is available online at www.nature.com/reprints. Correspondence and requests for materials should be addressed to Z.X. and C.W.W.

Competing financial interests

The authors declare no competing financial interests.

Methods

Stabilized self-injection-locked 658 nm pump laser. For the Franson measurements, good long- and short-term stability of the 658 nm pump laser is required, as this stability defines the coherence time of the two-photon state. This coherence time should be much longer than the path length difference (≈5 ns in our Franson measurements). We therefore designed and built a laser stabilized through self-injection-locking, in a configuration similar to the Littman–Metcalf cavity. With its single spatial mode, the longitudinal modes are selected through a diffraction grating (first order back into the diode; zeroth order as output) with an achieved mode-rejection ratio of more than 30 dB. Three temperature controllers are used to stabilize the doubly-enclosed laser system and a low-noise controller from Vescent Photonics (D2-105) drives the laser diode. With this design, a 2 MHz stability is achieved for 200 s measurement and integration timescales, as confirmed with the Franson interferometer. For longer timescales (12 h), a wavelength meter indicates ≈100 MHz drift. More details on the characterization, set-up and design are provided in Supplementary Section IV.

Franson interferometer. For the long-term phase-sensitive interference measurements, the fibre-based Franson interference needs to be carefully stabilized. Both interferometer arms are double-enclosed and sealed, and temperature-controlled with Peltier modules. Closed-loop piezoelectric control fine-tunes the arm2 delay. We designed and custom-built a pair of fibre collimators for fine focal adjustment, coupling and alignment. The double-pass delay line insertion loss is less than 0.4 ± 0.05 dB over the entire 27 mm delay-travel range (up to 360 ps in the reflected double-pass configuration). To verify the Franson interferometer stability, arm1 and arm2 are connected in series, and the interference visibility is observed up to 49.8 ± 1.0% for both short and long term, near or right at the 50% classical limit. The delay-temperature tuning transduction is quantified at 127 as per mK. More details on the characterization, set-up and design are provided in Supplementary Section III.

nature photonics

SUPPLEMENTARY INFORMATION

DOI: 10.1038/NPHOTON.2015.110

Harnessing high-dimensional hyperentanglement through a biphoton frequency comb

Zhenda Xie[1,2], Tian Zhong[3], Sajan Shrestha[2], XinAn Xu[2], Junlin Liang[2],Yan-Xiao Gong[4], Joshua C. Bienfang[5], Alessandro Restelli[5], Jeffrey H. Shapiro[3], Franco N. C. Wong[3], and Chee Wei Wong[1,2]

[1] *Mesoscopic Optics and Quantum Electronics Laboratory, University of California, Los Angeles, CA 90095*

[2] *Optical Nanostructures Laboratory, Columbia University, New York, NY 10027*

[3] *Research Laboratory of Electronics, Massachusetts Institute of Technology, Cambridge, MA 02139*

[4] *Department of Physics, Southeast University, Nanjing, 211189, People's Republic of China*

[5] *Joint Quantum Institute, University of Maryland and National Institute of Standards and Technology, Gaithersburg, Maryland 20899, USA*

I. Theory of two-photon interference of the high-dimensional biphoton frequency comb

Considering the Hong-Ou-Mandel (HOM) interference at an ideal 50:50 coupler, we can write the electric field operators at the two detectors D_1 and D_2 as

$$\hat{E}_1(t)=\frac{1}{\sqrt{2}}\left[\hat{E}_s(t)+\hat{E}_i(t+\delta T)\right],\quad \hat{E}_2(t)=\frac{1}{\sqrt{2}}\left[\hat{E}_s(t)-\hat{E}_i(t+\delta T)\right], \tag{1}$$

with the field operators before the HOM interferometer $\hat{E}_k(t)$, ($k=s,i$) given by

$$\hat{E}_k(t)=\frac{1}{\sqrt{2\pi}}\int d\omega\hat{a}_k(\omega)e^{-i\omega t}, \tag{2}$$

where δT is the arrival time difference for the signal and idler photons from the crystal to the coupler. Then the two-photon coincidence detection rate is expressed as

$$R_{12} \propto \int_{T_g} d\tau G_{12}^{(2)}(t, t+\tau), \tag{3}$$

with the correlation function given by

$$G_{12}^{(2)}(t, t+\tau) = \langle \psi | \hat{E}_1^\dagger(t) \hat{E}_2^\dagger(t+\tau) \hat{E}_2(t+\tau) \hat{E}_1(t) | \psi \rangle = \left| \langle 0 | \hat{E}_2(t+\tau) \hat{E}_1(t) | \psi \rangle \right|^2, \tag{4}$$

where T_g represents the timing between the detection gates. Here we assume the pump light is an ideal continuous-wave laser and thus neglect the average over the pump field. Substituting Eqs. (1), (2) and the spontaneous parametric downconverted (SPDC) state into Eq. (4) we obtain

$$G_{12}^{(2)}(t, t+\tau) \propto \left| g(\tau + \delta T) - g(-\tau + \delta T) \right|^2, \tag{5}$$

where we define $g(t) \equiv \int \Phi(\Omega) e^{i\Omega t} d\Omega$ and $\Phi(\Omega)$ denotes the spectrum amplitude. As $T_g >> T_c$, where T_c is the biphoton correlation time. The time integral range in Eq. (3) can be extended to (-∞, +∞). Then after the time integral we obtain the coincidence rate

$$\begin{aligned} R_{12} &\propto 1 - \mathrm{Re}\left[\int g^*(\tau) g(\tau + \delta T) d\tau \right] \Big/ \int |g(\tau)|^2 d\tau \\ &\propto 1 - \mathrm{Re}\left[\int \Phi(-\Omega) \Phi(\Omega) e^{2i\Omega\delta T} d\Omega \right] \Big/ \int |\Phi(\Omega)|^2 d\Omega \end{aligned} \tag{6}$$

For our source, the spectrum amplitude $\Phi(\Omega)$ has the following form

$$\Phi(\Omega) = \sum_{m=-N}^{N} f'(\Omega) h(\Omega) f(\Omega - m\Delta\Omega) = \sum_{m=-N}^{N} \frac{\mathrm{rect}(\Omega / B)\,\mathrm{sinc}(A\Omega)}{(\Delta\omega)^2 + (\Omega - m\Delta\Omega)^2}, \tag{7}$$

where $f'(\Omega) = \mathrm{sinc}(A\Omega)$ is the phase matching spectrum function, with the full width at half maximum (FWHM) as 2.78 / A, and $h(\Omega) = \mathrm{rect}(\Omega / B) = \begin{cases} 1, & |\Omega / B| \le 1/2 \\ 0, & |\Omega / B| > 1/2 \end{cases}$ is the rectangular spectrum function resulting from the FBG, with B denoting the width. The fiber Fabry-Perot cavity (FFPC) has a Lorentzian spectrum bin function characterized by: $f(\Omega) = f_s(\Omega) f_i(\Omega) = 1/[(\Delta\omega + i\Omega)(\Delta\omega - i\Omega)] = 1/[(\Delta\omega)^2 + \Omega^2]$, where $\Delta\Omega$ is the spacing between the frequency bins and $2\Delta\omega$ denotes the FWHM of each frequency bin. Corresponding to our measurements, we evaluate our theory using the following parameter values: A = 2.78 / (2π ×

245 GHz) = 1.81 ps, $B = 2\pi \times 346$ GHz $= 2.2 \times 10^{12}$ rad/s, $\Delta\Omega = 2\pi \times 15.15$ GHz $= 95.2 \times 10^{10}$ rad/s, and $\Delta\omega = 2\pi \times 1.36$ GHz / 2 $= 4.27 \times 10^{9}$ rad/s. The spectrum density $|\Phi(\Omega)|^2$ can be described by

$$|\Phi(\Omega)|^2 = \sum_{m=-N}^{N} |f'(\Omega)|^2 |h(\Omega)|^2 |f(\Omega - m\Delta\Omega)|^2 = \sum_{m=-N}^{N} \frac{\mathrm{sinc}^2(A\Omega)\,\mathrm{rect}(\Omega/B)}{[(\Delta\omega)^2 + (\Omega - m\Delta\Omega)^2]^2}, \tag{8}$$

where we have neglected the overlaps among the frequency bins since $\Delta\Omega >> 2\Delta\omega$. Moreover, as the FWHM of $|f'(\Omega)|^2$, 2.78 / A is much larger than $2\Delta\omega$ and the width of $|h(\Omega)|^2$, and $B >> 2\Delta\omega$, we can make the following approximation

$$\begin{aligned} |\Phi(\Omega)|^2 &\cong \sum_{m=-N}^{N} |f'(Am\Delta\Omega)|^2 |h(m\Delta\Omega)|^2 |f(\Omega - m\Delta\Omega)|^2 \\ &= \sum_{m=-N}^{N} \frac{\mathrm{sinc}^2(Am\Delta\Omega)\,\mathrm{rect}(m\Delta\Omega/B)}{[(\Delta\omega)^2 + (\Omega - m\Delta\Omega)^2]^2} = \sum_{m=-N_0}^{N_0} \frac{\mathrm{sinc}^2(Am\Delta\Omega)}{[(\Delta\omega)^2 + (\Omega - m\Delta\Omega)^2]^2}, \end{aligned} \tag{9}$$

where $N_0 = \lfloor B/(2\Delta\Omega) \rfloor = 11$ is the integer part of $B / 2\Delta\Omega$. Thus we can obtain

$$\int |\Phi(\Omega)|^2 \, d\Omega = \sum_{m=-N_0}^{N_0} \int d\Omega \frac{\mathrm{sinc}^2(Am\Delta\Omega)}{[(\Delta\omega)^2 + (\Omega - m\Delta\Omega)^2]^2} = \frac{\pi}{2(\Delta\omega)^3} \sum_{m=-N_0}^{N_0} \mathrm{sinc}^2(Am\Delta\Omega). \tag{10}$$

$$\begin{aligned} \int \Phi(-\Omega)\Phi(\Omega) e^{2i\Omega\delta T} d\Omega &= \int |\Phi(\Omega)|^2 \, e^{2i\Omega\delta T} d\Omega \\ &= \sum_{m=-N_0}^{N_0} \int d\Omega \frac{\mathrm{sinc}^2(Am\Delta\Omega)}{[(\Delta\omega)^2 + (\Omega - m\Delta\Omega)^2]^2} e^{2i\Omega\delta T} \\ &= \frac{\pi e^{-2\Delta\omega|\delta T|}(1 + 2\Delta\omega\,|\,\delta T\,|)}{2(\Delta\omega)^3} \sum_{m=-N_0}^{N_0} \mathrm{sinc}^2(Am\Delta\Omega) e^{2im\Delta\Omega\delta T} \\ &= \frac{\pi e^{-2\Delta\omega|\delta T|}(1 + 2\Delta\omega\,|\,\delta T\,|)}{2(\Delta\omega)^3} \left[2\sum_{m=1}^{N_0} \mathrm{sinc}^2(Am\Delta\Omega) \cos(2m\Delta\Omega\delta T) + 1 \right]. \end{aligned} \tag{11}$$

Then through Eq. (6) we arrive at the coincidence rate as

$$R_{12} \propto 1 - \frac{e^{-2\Delta\omega|\Delta T|}(1 + 2\Delta\omega\,|\,\delta T\,|)}{\sum_{m=-N_0}^{N_0} \mathrm{sinc}^2(Am\Delta\Omega)} \left[2\sum_{m=1}^{N_0} \mathrm{sinc}^2(Am\Delta\Omega) \cos(2m\Delta\Omega\delta T) + 1 \right]. \tag{12}$$

We model the second-order correlation based on our experimental parameters. The coincidence rate versus δT in the range of {-320 ps, 320 ps} is plotted in Supplementary Figure S1. We can see the interference fringe is a multi-dip pattern, with the dip revival period of about 33.2 ps, matching the 33.4 ps in our measurements. The linewidth of each Hong-Ou-Mandel dip and the fall-off in visibility for increasing ±*k* bins from the zero delay point also matches with the experimental observations.

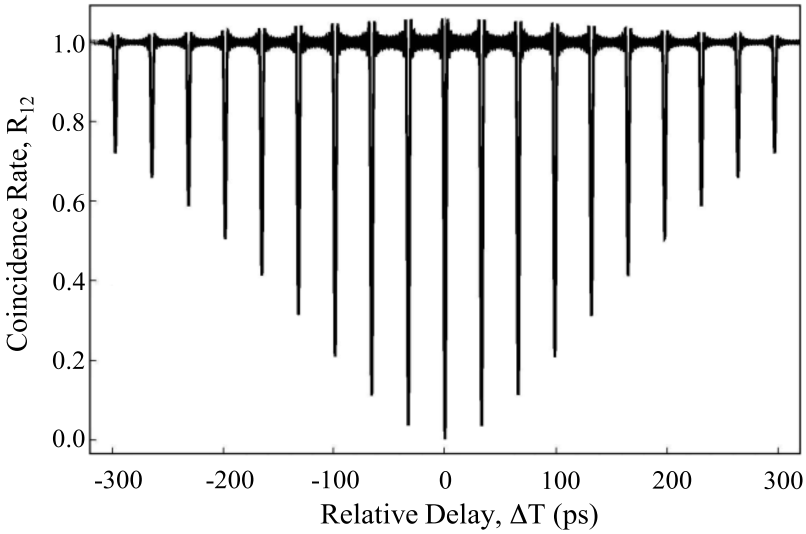

Supplementary Figure S1 | Modeling of Hong-Ou-Mandel interference revivals for the high-dimensional biphoton frequency comb. The coincidence counting rate R_{12} as a function of δT, the arrival time difference between the signal and idler photons. The fall-off in the revived visibility away from the zero delay point arises from the Lorentzian lineshape of the SPDC individual photons after passing through the cavity.

In the experiment, the bandwidth of FBG is more than that of the phase matching. It is reasonable to assume an infinite number of frequency bins, i.e., $N \rightarrow \infty$, and making the replacement of $\delta T = \delta T' + kT/2$, where $T = 2\pi/\Delta\Omega$, $-A < \delta T' \leq T/2 - A$, and k is an integer number, we can simplify Eq. (12) to

$$R_{12}(\delta T' + kT/2) \propto \begin{cases} 1 - e^{-2\Delta\omega|\delta T' + k\pi/\Delta\Omega|}(1 + 2\Delta\omega\,|\,\delta T' + k\pi/\Delta\Omega\,|)(1 - |\,\delta T'\,|/A) & -A < \delta T' < A, \\ 0 & A \le \delta T' \le \pi/\Delta\Omega - A. \end{cases} \qquad (13)$$

We can see the dip revival period is $T_R = \pi/\Delta\Omega \approx 33.2$ ps (or *T*/2) and the visibility of the *k*-th order dip is $e^{-2|k|\pi\Delta\omega/\Delta\Omega}(1 + 2\,|\,k\,|\,\pi\Delta\omega/\Delta\Omega)$. We note that the recurrence is at *T/2* instead of at *T* in our prior analysis where the beamsplitter was moved [J. H. Shapiro, *Technical Digest of Topical Conference on Nonlinear Optics*, p.44, FC7-1, Optical Society of America (2002)]. With the beamsplitter shift, the transmitted signal and idler beams do not experience an advance or a delay, but one reflected beam is advanced while the other is delayed. In our case, only the idler beam is delayed, giving rise to the *T/2* recurrence in the coincidences as detailed above.

II. Theory of Franson interference of the high-dimensional biphoton frequency comb

The electric field operators at the two detectors D_1 and D_2 can be expressed as

$$\hat{E}_1(t) = \frac{1}{2}\left[\hat{E}_s(t) + \hat{E}_s(t - \Delta T_1)\right], \quad \hat{E}_2(t) = \frac{1}{2}\left[\hat{E}_i(t) + \hat{E}_i(t - \Delta T_2)\right], \qquad (14)$$

with the field detectors before the Franson interferometer $\hat{E}_k(t)$, $(k = s, i)$ given by

$$\hat{E}_k(t) = \frac{1}{\sqrt{2\pi}}\int d\omega\,\hat{a}_k(\omega)e^{-i\omega t}, \qquad (15)$$

where $\Delta T_1, \Delta T_2$ are the unbalanced arm differences. Then the two-photon coincidence detection rate can be described by

$$R_{12} \propto \int_{T_g} d\tau\, G_{12}^{(2)}(t, t+\tau), \qquad (16)$$

with the correlation function given by

$$G_{12}^{(2)}(t, t+\tau) = \left\langle \psi \left| \hat{E}_1^{\dagger}(t)\hat{E}_2^{\dagger}(t+\tau)\hat{E}_2(t+\tau)\hat{E}_1(t) \right| \psi \right\rangle = \left| \left\langle 0 \left| \hat{E}_2(t+\tau)\hat{E}_1(t) \right| \psi \right\rangle \right|^2, \qquad (17)$$

where T_g represent the timing between the detection gates. Here we assume the pump light is an ideal continuous-wave laser and thus neglect the average over the pump field. Substituting Eqs. (1), (2) and the SPDC state into Eq. (4), we obtain

$$G_{12}^{(2)}(t,t+\tau)=\left|G(t,t)+G(t-\Delta T_1,t-\Delta T_2)+G(t-\Delta T_1,t)+G(t,t-\Delta T_2)\right|^2, \tag{18}$$

with

$$G(t_1,t_2)=\frac{1}{8\pi}e^{-i\omega_p(t_1+t_2+\tau)/2}\int\Phi(\Omega)e^{i\Omega(t_2-t_1+\tau)}d\Omega=\frac{1}{8\pi}e^{-i\omega_p(t_1+t_2+\tau)/2}g(t_2-t_1+\tau), \tag{19}$$

where $\Phi(\Omega)$ denotes the spectrum amplitude and we define $g(t)\equiv\int\Phi(\Omega)e^{i\Omega t}d\Omega$. Then we may rewrite Eq. (5) as

$$\begin{aligned}G_{12}^{(2)}(t,t+\tau)\propto\Big|&e^{-i\omega_p\tau/2}g(\tau)+e^{-i\omega_p(\tau-\Delta T_1-\Delta T_2)/2}g(\tau+\Delta T_1-\Delta T_2)\\&+e^{-i\omega_p(\tau-\Delta T_1)/2}g(\tau+\Delta T_1)+e^{-i\omega_p(\tau-\Delta T_2)/2}g(\tau-\Delta T_2)\Big|^2.\end{aligned} \tag{20}$$

As we have noted, $\Delta T_1,\Delta T_2$ are much larger than the single-photon coherence time T_c, i.e., the range of the function $g(t)$, so there is only one non-zero cross term in Eq. (20). Thus we obtain

$$\begin{aligned}G_{12}^{(2)}(t,t+\tau)\propto&\left|g(\tau)\right|^2+\left|g(\tau+\Delta T_1-\Delta T_2)\right|^2+\left|g(\tau+\Delta T_1)\right|^2+\left|g(\tau-\Delta T_2)\right|^2\\&+2\,\mathrm{Re}[e^{i\omega_p(\Delta T_1+\Delta T_2)/2}g^*(\tau)g(\tau+\Delta T_1-\Delta T_2)].\end{aligned} \tag{21}$$

Since ΔT_1, $\Delta T_2 >> T_g$, the coincidence detection system can resolve the short and long paths and thus the two terms $\left|g(\tau+\Delta T_1)\right|^2$, $\left|g(\tau-\Delta T_2)\right|^2$ have no contribution to the coincidence rate. Moreover, as $T_g >> T_c$, the time integral range in Eq. (3) can be extended as $(-\infty,+\infty)$. Then after the time integral we obtain the coincidence rate

$$R_{12}\propto 1+\left|\Gamma(\Delta T)\right|\cos[[\omega_p\Delta T/2+\omega_p\Delta T_2+\varphi], \tag{22}$$

where $\Delta T=\Delta T_1-\Delta T_2$, and

$$\begin{aligned}\Gamma(\Delta T)&=\int g^*(\tau)g(\tau+\Delta T)d\tau\Big/\int\left|g(\tau)\right|^2d\tau\\&=\int\Phi(-\Omega)\Phi(\Omega)e^{i\Omega\Delta T}d\Omega\Big/\int\left|\Phi(\Omega)\right|^2d\Omega\Big|=\Gamma(\Delta T)\Big|e^{i\varphi}.\end{aligned} \tag{23}$$

For our source, the spectrum amplitude $\Phi(\Omega)$ has the following form

$$\Phi(\Omega) = \sum_{m=-N}^{N} f'(\Omega)h(\Omega)f(\Omega - m\Delta\Omega) = \sum_{m=-N}^{N} \frac{\mathrm{rect}(\Omega/B)\,\mathrm{sinc}(A\Omega)}{(\Delta\omega)^2 + (\Omega - m\Delta\Omega)^2}, \tag{24}$$

Then we can write the spectrum density $|\Phi(\Omega)|^2$ as

$$|\Phi(\Omega)|^2 = \sum_{m=-N}^{N} |f'(\Omega)|^2 |h(\Omega)|^2 |f(\Omega - m\Delta\Omega)|^2 = \sum_{m=-N}^{N} \frac{\mathrm{sinc}^2(A\Omega)\,\mathrm{rect}(\Omega/B)}{[(\Delta\omega)^2 + (\Omega - m\Delta\Omega)^2]^2}, \tag{25}$$

where we have neglected the overlaps among the frequency bins since $\Delta\Omega >> 2\Delta\omega$. Moreover, as the FWHM of $|f'(\Omega)|^2$, $2.78 / A >> 2\Delta\omega$, and the width of $|h(\Omega)|^2$, $B >> 2\Delta\omega$, we can make the following approximation

$$\begin{aligned} |\Phi(\Omega)|^2 &\cong \sum_{m=-N}^{N} |f'(Am\Delta\Omega)|^2 |h(m\Delta\Omega)|^2 |f(\Omega - m\Delta\Omega)|^2 \\ &= \sum_{m=-N}^{N} \frac{\mathrm{sinc}^2(Am\Delta\Omega)\,\mathrm{rect}(m\Delta\Omega/B)}{[(\Delta\omega)^2 + (\Omega - m\Delta\Omega)^2]^2} = \sum_{m=-N_0}^{N_0} \frac{\mathrm{sinc}^2(Am\Delta\Omega)}{[(\Delta\omega)^2 + (\Omega - m\Delta\Omega)^2]^2}, \end{aligned} \tag{26}$$

where $N_0 = \lfloor B/(2\Delta\Omega) \rfloor = 11$ is the integer part of $B/(2\Delta\Omega)$. Thus we can obtain

$$\int |\Phi(\Omega)|^2 d\Omega = \sum_{m=-N_0}^{N_0} \int d\Omega \frac{\mathrm{sinc}^2(Am\Delta\Omega)}{[(\Delta\omega)^2 + (\Omega - m\Delta\Omega)^2]^2} = \frac{\pi}{2(\Delta\omega)^3} \sum_{m=-N_0}^{N_0} \mathrm{sinc}^2(Am\Delta\Omega). \tag{27}$$

$$\begin{aligned} \int \Phi(-\Omega)\Phi(\Omega) e^{i\Omega\Delta T} d\Omega &= \int |\Phi(\Omega)|^2 e^{i\Omega\Delta T} d\Omega \\ &= \sum_{m=-N_0}^{N_0} \int d\Omega \frac{\mathrm{sinc}^2(Am\Delta\Omega)}{[(\Delta\omega)^2 + (\Omega - m\Delta\Omega)^2]^2} e^{i\Omega\Delta T} \\ &= \frac{\pi e^{-\Delta\omega|\Delta T|}(1 + \Delta\omega|\Delta T|)}{2(\Delta\omega)^3} \sum_{m=-N_0}^{N_0} \mathrm{sinc}^2(Am\Delta\Omega) e^{im\Delta\Omega\Delta T} \\ &= \frac{\pi e^{-\Delta\omega|\Delta T|}(1 + \Delta\omega|\Delta T|)}{2(\Delta\omega)^3} \left[2\sum_{m=1}^{N_0} \mathrm{sinc}^2(Am\Delta\Omega)\cos(m\Delta\Omega\Delta T) + 1 \right]. \end{aligned} \tag{28}$$

Then through Eqs. (6) and (10), we can write the coincidence rate as

$$\begin{aligned} R_{12} \propto 1 + &\frac{e^{-\Delta\omega|\Delta T|}(1 + \Delta\omega|\Delta T|)}{\sum_{m=-N_0}^{N_0} \mathrm{sinc}^2(Am\Delta\Omega)} \left[2\sum_{m=1}^{N_0} \mathrm{sinc}^2(Am\Delta\Omega)\cos(m\Delta\Omega\Delta T) + 1 \right] \\ &\times \cos[\omega_p(\Delta T/2 + \Delta T_2)]. \end{aligned} \tag{29}$$

Since $\omega_p/2 = \pi c/\lambda_p = 1.43 \times 10^{12}$ rad/s >> $\Delta\omega$, $\Delta\Omega$, the term $\cos[\omega_p(\Delta T/2 + \Delta T_2)]$ is the fast collision part of the interference fringe with the other part determining the fringe envelope. We can simulate our experimental results with the theoretical parameters above and for $\Delta T_2 = 5$ ns.

If we consider a large number of frequency bins such as in our measurements, i.e., $N \to \infty$, and make the replacement of $\Delta T = \Delta T' + kT$, where $-2A < \Delta T' \leq T - 2A$, and k is an integer number, we can simplify Eq. (16) to

$$R_{12}(\Delta T' + kT) \propto \begin{cases} 1 + e^{-\Delta\omega|\Delta T' + 2k\pi/\Delta\Omega|}(1 + \Delta\omega|\Delta T' + 2k\pi/\Delta\Omega|)[1 - |\Delta T'|/(2A)] & \\ \quad \times \cos[\omega_p(\Delta T'/2 + k\pi/\Delta\Omega + \Delta T_2)] & -2A < \Delta T' < 2A, \\ 0 & 2A \leq \Delta T' \leq 2\pi/\Delta\Omega - 2A. \end{cases} \tag{30}$$

The fringe envelope of the coincidence rate versus ΔT is plotted in Supplementary Figure S2. We see that the interference fringe has a recurrent envelope that falls off away from the zero delay point due to the Lorentzian lineshape of the FFPC. The recurrence period T is about 66 ps and agrees well with repetition time of the biphoton frequency comb, i.e., the round trip time of the FFPC. The maximum visibility at the k-th order peaks can be found to be $e^{-2|k|\pi\Delta\omega/\Delta\Omega}(1 + 2|k|\pi\Delta\omega/\Delta\Omega)$. This gives an envelope visibility which matches well with the experimental measurements.

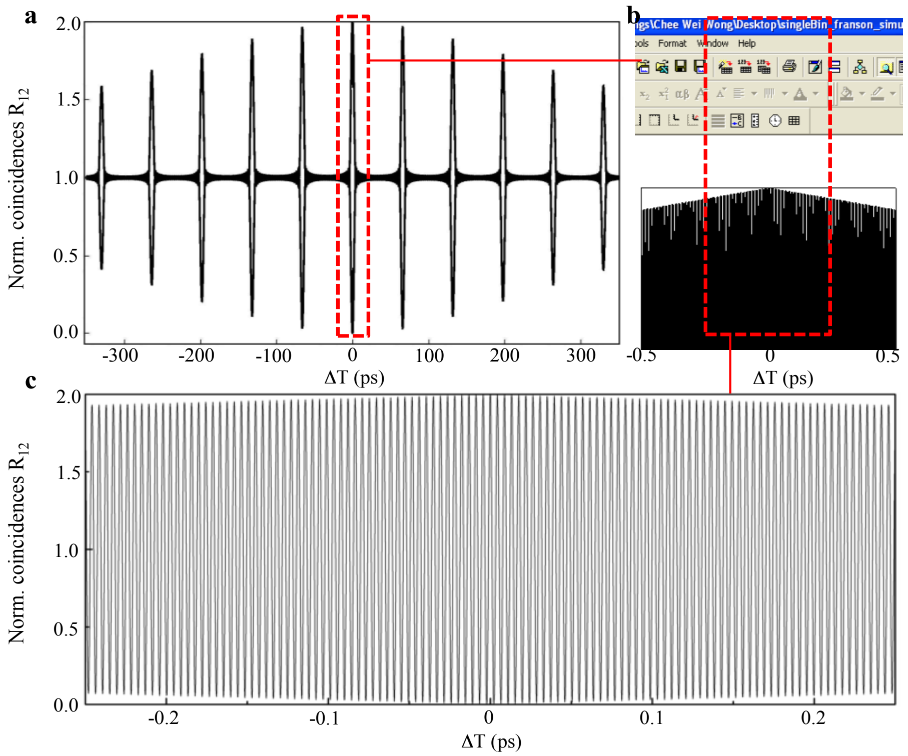

Supplementary Figure S2 | Theory of Franson interference revival for the high-dimensional biphoton frequency comb. **a,** The envelope of coincidence counting rates R_{12} plotted as a function of ΔT. The interference has a recurrent envelope that falls off away from the zero delay point, arising from the finite coherence time of the single frequency bin**. b,** zoom-in of Franson interferences for the first time bin. **c,** Further zoom-in of the Franson interferences for the first time bin. The high-frequency interference oscillations arise from the phase.

III. Characterization of Franson interferometer long-term stability

In our measurement, the fiber-based Franson interferometer needs to be stabilized at the wavelength level over long term for the phase sensitive interference measurements. All components are fixed on the aluminum housing with thermal conductive epoxy for good thermal contact. Both interferometer arms are temperature-controlled with Peltier modules and sealed in aluminum enclosures which themselves are also temperature stabilized. The delay line in *arm2* is based on a miniaturized linear stage with closed-loop piezoelectric motor control (CONEX-AG-

LS25-27P, Newport Corporation). The two fiber collimators are custom-built in-house with fine focal adjustment for optimized pair performance and epoxied on the housing. The delay line is aligned so that the double-pass insertion loss is less than 0.4 ± 0.05 dB throughout the whole travel range of 27 mm of the linear stage. The effective delay range is about 0 to 360 ps for the reflected light, considering the double-pass optical path configuration and reflector setup.

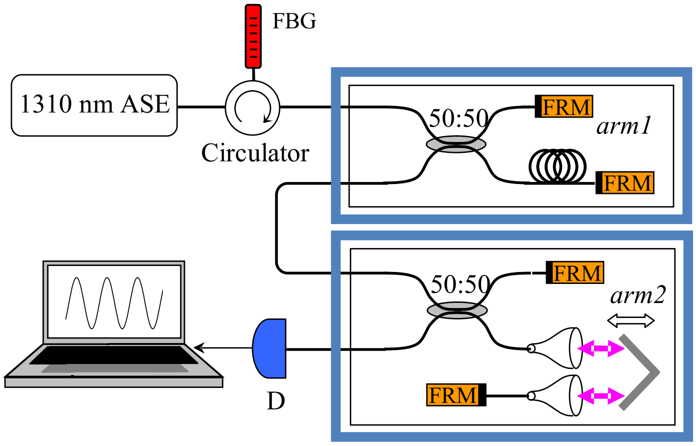

Supplementary Figure S3 | Long-term stability test of the Franson interferometer. *Arm1* and *arm2* are connected in series for the classical interference test. Both interferometers are double temperature controlled, and the delay line in *arm2* is closed-loop piezoelectrically controlled. Dual collimators are custom-built in-house with fine focal adjustment and optimized performance. Fine-tuned alignment is such that the double-pass insertion loss is less than 0.4 dB throughout the whole 27 mm travel range and up to 360 ps optical delay.

We have verified the stability of the Franson interferometer using classical interference before the quantum correlation measurements. The setup is shown in Supplementary Figure S3. The light is from a 1310 nm amplified spontaneous emission (ASE) source (S5FC1021S, Thorlabs Inc.), and filtered with the same filter sub-assembly that is used in the biphoton frequency comb generation. The two arms are connected in series so that classical interference occurs between the events of passing long path of *arm1*, short path of *arm2*, and short path of *arm1*, long path of *arm2*, while $\Delta T_1 = \Delta T_2$. The visibility of this interference is limited to 50%, because of other events that contribute to the background. The intensity of the output is measured using a photodiode (PDA20CS, Thorlabs Inc.), while tuning the temperature of *arm1*. The result is shown in Supplementary Figure S4. The observed interferences agree well with a sinusoidal fit, and the visibility is 49.8 ± 1.0%, near or right at the classical limit over long measurement time periods. This indicates the Franson interferometer is well stabilized. We can also obtain the delay coefficient for this temperature tuning, which is observed to be 127 attoseconds per mK based on the fringe period when the temperature is tuned.

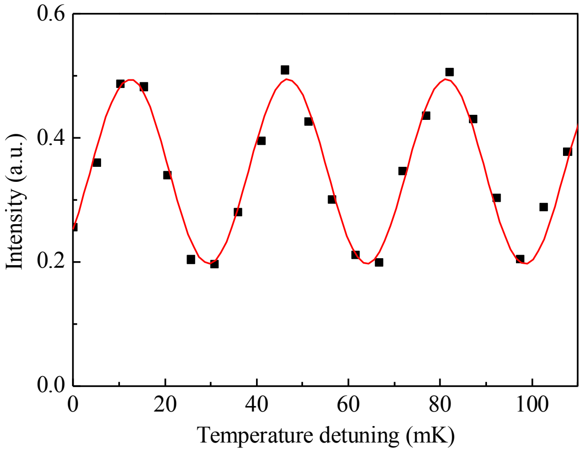

Supplementary Figure S4 | Classical interference visibility of the stabilized coupled interferometers. Temperature of *arm1* is tuned and the input is a 1310 nm ASE source. The temperature-delay sensitivity is observed to be 127 attoseconds per mK.

IV. Stabilization of the pump laser in Franson interference

The Franson interference requires high stability – both short and long term – of the pump laser, which defines the two-photon coherence time of the two-photon state. The coherence time of the pump laser should be much longer than the path length difference. This path length difference is 5 ns in our experiment. Therefore, we custom-built a stabilized laser at 658 nm using self-injection-locking. The setup is shown in Supplementary Figure S5a, which is similar to a Littman–Metcalf configuration external diode laser. The laser source that we use is a standard Fabry-Perot laser diode with center wavelength around 658 nm (QLD-658-20S). It is spatially single-mode, but has multiple longitudinal modes without feedback. A diffraction grating is used for the longitudinal mode selection. The laser beam is first collimated onto the grating. The first-order diffraction reflects off a tunable mirror back into the diode through the grating. The zeroth order diffraction from the grating is used as the output. Because of the grating, we succeed in achieving single-mode lasing, with a mode-rejection ratio over 30 dB. The whole setup is isolated with double enclosures. The inner enclosure is made from aluminum and temperature-stabilized. The outer laser housing is also a solid piece of aluminum that is temperature-stabilized. A third temperature stabilization is applied to the diode.

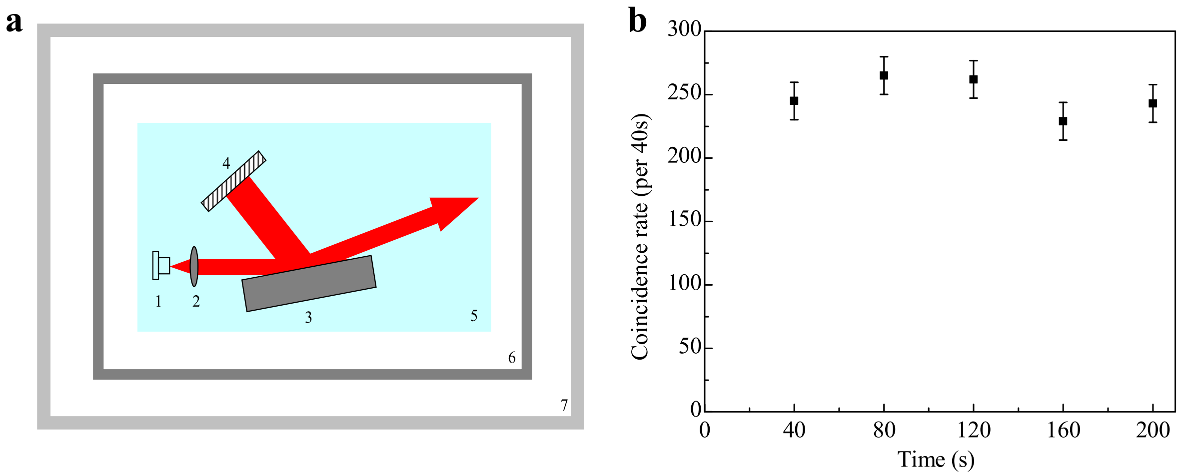

Supplementary Figure S5 | Stabilized 658 nm pump laser with self-injection locking and characterization through Franson-type interferometer. a, Layout schematic of custom-built 658 nm stabilized laser. 1, 658 nm Fabry-Perot laser diode with temperature stabilization; 2, collimating lens; 3, diffraction grating; 4, high-reflection mirror; 5, temperature-stabilized laser housing; 6, internal enclosure with temperature stabilization; 7, external enclosure. **b,** Franson interference measurement to demonstrate pump laser stability, with the interferometer tuned to the 0th time bin. Measurement is made at 6 mW pump power. The measured deviation of the counting rate is about 5%, with the coincidence measurements taken every 40 seconds, which corresponds to a 2 MHz drift of the pump laser. The long term drift, over 12 hours, is less than 100 MHz.

The current source for the diode is a low-noise laser diode controller (D2-105, Vescent Photonics, Inc.). With these stabilizations, we achieve a free-running wavelength drift of the 658 nm laser at less than 2 MHz within 200 seconds, which is an integration time step for the Franson measurement. The laser linewidth is measured classically with the Franson-type interferometer setup. The pump power is about 6 mW in the measurement. We tune the interferometer to the 0th time bin. ΔT is set such that the coincidence counting rate is about the middle of the sinusoidal fringe, which gives the best sensitivity to the pump drift. The coincidence counting rate is taken every 40 seconds, and the result is shown in Supplementary Figure S5b. The measured deviation of counting rate is about 5%, which corresponds to a pump drift of 2 MHz. The long-term drift is less than 100 MHz within 12 hours (measured with a wavelength meter, HighFinesse WS-7).

V. Measurements of Hong-Ou-Mandel revival of the high-dimensional biphoton frequency comb

In the main text, we used an InGaAs/InP single-photon detector D_2 with ~ 2.5 ns effective gate width for the measurements, so that the detection gate widows of D_1 and D_2 are always well-overlapped through the scanning range of relative delay.

Figure S6 illustrates another example of the Hong-Ou-Mandel revival when using an effective detector gate width of ≈ 400 ps. The maximum visibility of the central dip can be enhanced to 96.1%, because of the reduced accidental coincidence possibility. That visibility becomes 97.8% after subtracting the accidental coincidence counts. We note that, in the accidentals subtraction, the estimated double pairs are still included in the counts for the best estimate of the visibility. The single-photon counting rate remains constant during the measurement. However, here the background of the coincidence counting rate drops as the relative delay increases (see Supplementary Figure S6a). This drop is from the temporal overlap reduction for the gating of D_1 and D_2 at large relative delays of the HOM interferometer.

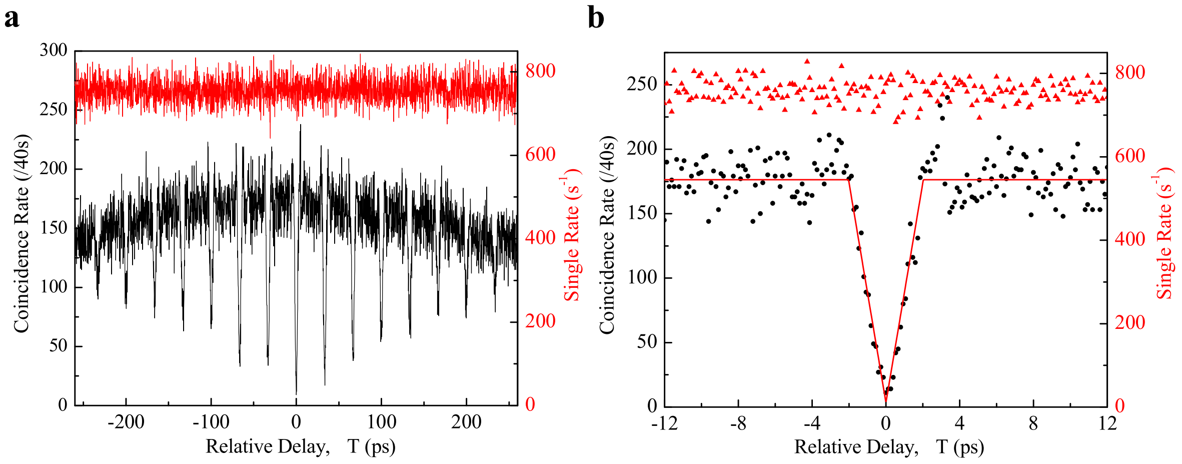

Supplementary Figure S6 | HOM measurement with single-photon detectors with an effective gate width of ≈ 400 ps. a, Coincidence and single counting rates as a function of the relative delay between the two arms of the HOM interferometer. The background of the coincidence counting rate drops because of the reduced overlap between the detection windows of D_1 and D_2. **b,** Zoom-in coincidence and single counting rate around zero relative delay between the two arms. The visibility is measured to be 96.1 %, or 97.8 % after subtracting the accidental coincidence counts.

VI. Polarization entanglement measurements of the high-dimensional biphoton frequency comb

Before the hyperentanglement measurements, we test the polarization entanglement alone for the hyperentangled state. Supplementary Figure S7a shows the experiment setup. We mix the signal and idler photons on a 50:50 fiber coupler with orthogonal polarizations. By keeping the relative delay $\delta\tau = 0$, the signal and idler photons are well-overlapped temporally for the interference. We present a measurement for the polarization entanglement by measuring the coincidence counting rates while changing the angle of P2, when P1 was set at 45^o and 90^o, respectively. As shown in Supplementary Figure S7b, both results fit well with sinusoidal curves, with visibilities of 91.2 ± 1.6% and 93.0 ± 1.3%, which violate the Bell inequality by 12.8 and 17.7 standard deviations, respectively. This indicates the high-dimensional polarization entangled state $|\psi\rangle = \sum_{m=-N}^{N} |\omega_p/2 + m\Delta\Omega\rangle_1 |\omega_p/2 - m\Delta\Omega\rangle_2 \otimes (|H\rangle_1 |V\rangle_2 + |V\rangle_1 |H\rangle_2)$ is generated with high quality. Hence, in addition to the 4 frequency bits, the biphoton frequency comb also has polarization entanglement for use as a high-dimensional quantum communications platform.

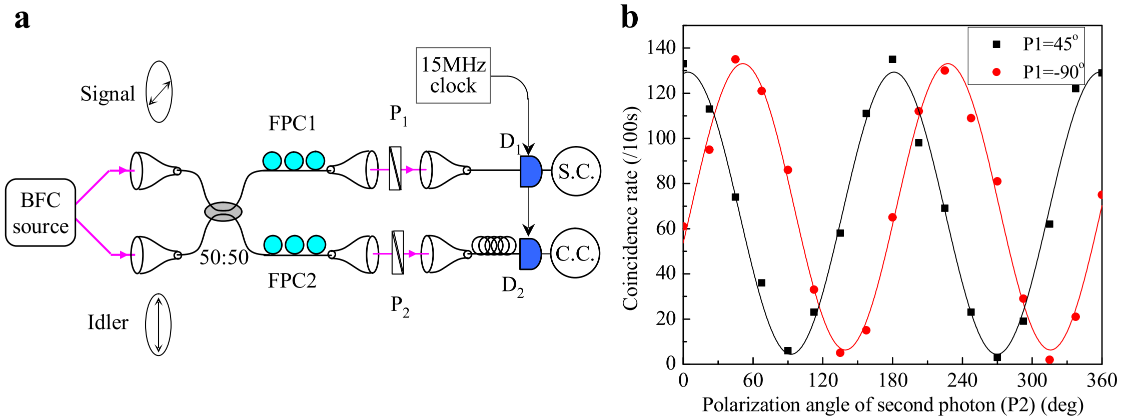

Supplementary Figure S7 | Polarization entanglement measurements of the high-dimensional biphoton frequency comb. a, Illustrative experimental scheme. The signal and idler photons are sent to a 50:50 fiber coupler with orthogonal polarizations for the generation of polarization entanglement. P: polarizer; S.C.: single counts; C.C.: coincidence counts. **b**, Polarization entanglement measurements with P1 fixed at 45$^{\text{o}}$ and 90$^{\text{o}}$. In both cases, we measured the coincidence counting rates at the two outputs while changing P2 from 0$^{\text{o}}$ to 360$^{\text{o}}$. As shown by the black line (for P1 = 45$^{\text{o}}$) and red line (for P1 = 90$^{\text{o}}$), both measured results fit well with sinusoidal curves, with accidentals-subtracted visibilities of 91.2 % and 93.0 %, respectively.

VII. High-dimensional hyperentanglement and Bell inequality statistics

We performed a series of hyperentangled measurements of the biphoton frequency comb with the visibilities summarized in Table 1 below, for the different P1 settings and different time-bin settings, across the energy-time basis and the polarization basis. The resulting standard deviation violation of the Bell inequality is computed correspondingly. Measurements are performed at 80-second integration times based on the tradeoff between the setup's long-term stability over the complete hyperentanglement measurements and sufficiently reduced standard deviations of the coincidence counts. The Clauser-Horne-Shimony-Holt (CHSH) *S* parameter is determined from the polarization analysis angle set of the ($|H\rangle|V\rangle+|V\rangle|H\rangle$) triplet state:

$$\mathrm{S}\equiv\left|-C(\pi/2,7\pi/8)+C(\pi/4,7\pi/8)+C(\pi/4,5\pi/8)+C(\pi/2,5\pi/8)\right| \tag{31}$$

Table 1 | Visibilities for the interference fringes in the high-dimensional hyperentanglement measurement and Bell inequality violations. "st.d." denotes standard deviation σ.

		Time bin #0	Time bin #1	Time bin #2	Time bin #3	Time bin #4
P1 = 45°, Polarization basis	Visibility V	82.9%	80.1%	77.3%	73.8%	77.3%
	V (dark counts subtracted)	96.3%	96.2%	95.9%	93.8%	95.8%
	Bell violation (by st.d. σ)	8.83	9.46	10.5	6.8	9.33
P1 = 45°, Energy-time basis	Visibility V	81.1%	74.1%	68.0%	60.0%	44.2%
	V (dark counts subtracted)	94.1%	87.5%	83.3%	74.7%	53.2%
	Bell violation (by st.d. σ)	7.34	5.19	4.83	2.12	none
P1 = 90°, Polarization basis	Visibility V	81.4%	76.6%%	75.8%	75.1%	75.3%
	V (dark counts subtracted)	96.9%	95.0%	95.8%	94.5%	95.7%
	Bell violation (by st.d. σ)	10.95	8.09	7.62	8.51	7.97
P1 = 90°, Energy-time basis	Visibility V	80.3%	72.3%	67.5%	59.4%	44.2%
	V (dark counts subtracted)	95.9%	89.0%	84.3%	73.6%	54.1%
	Bell violation (by st.d. σ)	7.87	8.34	5.67	1.92	none
CHSH *S* parameter		2.71	2.67	2.76	2.74	2.53

been successfully detected with single-lattice-site resolution at Harvard University, once again using Raman sideband cooling[12]. One important aspect is the fact that, due to rapid light-assisted collision processes in multiply occupied sites, such quantum gas microscopes are only sensitive to the parity of the on-site atom number. Although this can be a severe limitation for bosonic systems, it is less a problem for ultracold fermions when they occupy a single lattice band because Pauli's exclusion principle forbids multiple occupancy on a single site.

All three Fermi gas microscope experiments achieved a very good fidelity in the distinction of empty and unity occupied sites after illumination times between one and two seconds in which approximately 1,000 photons per atom were collected. However, an excellent optical detection signal-to-noise ratio is not the only important feature of a useful quantum gas microscope. Equally important is a low atom loss and low hopping rate during the illumination time. Both require efficient cooling to confine the atoms to the lowest onsite energy levels during the time they scatter light. One way to quantify these rates is to take successive images of the same atomic cloud and to directly 'watch' the atoms disappear or hop. All three research teams performed these measurements and demonstrated that low rates (a few per cent) can be achieved and, thus, that high-fidelity imaging of strongly correlated fermions can be realized. The highest demonstrated reconstruction fidelity of the parity signal is 95% (ref. 12).

In the three experiments an optical resolution slightly better than the wavelength of the imaging light (671 nm for lithium and 770 nm for potassium) is required to detect the atoms with single-lattice-site resolution. This is achieved by using high numerical aperture (>0.8) imaging techniques, which need to be compatible with an ultracold atom experiment carried out in an ultrahigh vacuum environment. The groups use different strategies to accomplish this. Whereas the Strathclyde team works with a highly specialized custom-designed objective that combines a high numerical aperture with a large working distance above one centimetre, the teams at Harvard and MIT prepare their two-dimensional gas a few micrometres away from a hemisphere in optical contact with the vacuum window. In both approaches the depth of focus is limited, such that high-resolution quantum gas microscopes are at present restricted to the detection of a single two-dimensional plane.

These imaging techniques pave the way towards a new generation of quantum gas experiments with fermions. The next step is to achieve low temperatures of the two-dimensional quantum gases under the microscopes. Here, the state of the art in other experiments is around 5% to 10% of the Fermi temperature. This requires the combination of the best (evaporative) cooling strategies with the quantum microscope set-ups. Once such cold temperatures have been achieved, the microscopes can be used to probe strongly correlated fermionic quantum gases with unprecedented resolution at the single atom level.

Further developments include the implementation of single-site manipulation techniques. These are ideally suited to study the response of the system to local quenches or to project arbitrary potentials onto the atoms. Even the simultaneous detection of two spin states might be implemented in the future, making the technique even more powerful for the study of quantum magnetism. Finally, quantum gas microscopy can also be used to study small sufficiently dilute continuous systems with high precision. In this case the optical lattices can be ramped up suddenly to freeze the atomic position for the subsequent single-atom-sensitive detection. ❐

Christian Groß is at the Max-Planck-Institut für Quantenoptik, Hans-Kopfermann-Straße 1, 85748 Garching, Germany.
e-mail: christian.gross@mpq.mpg.de

References

1. Nelson, K. D., Li, X. & Weiss, D. S. *Nature Phys.* **3,** 556–560 (2007).
2. Bakr, W. S., Gillen, J. I., Peng, A., Fölling, S. & Greiner, M. *Nature* **462,** 74–77 (2009).
3. Sherson, J. F. *et al. Nature* **467,** 68–72 (2010).
4. Miranda, M., Inoue, R., Okuyama, Y., Nakamoto, A. & Kozuma, M. *Phys. Rev.* A **91,** 063414 (2015).
5. Endres, M. *et al. Science* **334,** 200–203 (2011).
6. Cheneau, M. *et al. Nature* **481,** 484–487 (2012).
7. Fukuhara, T. *et al. Nature Phys.* **9,** 235–241 (2013).
8. Simon, J. *et al. Nature* **472,** 307–312 (2011).
9. Schauß, P. *et al. Nature* **491,** 87–91 (2012).
10. Haller, E. *et al. Nature Phys.* http://dx.doi.org/10.1038/nphys3403 (2015).
11. Cheuk, L. W. *et al. Phys. Rev. Lett.* **114,** 193001 (2015).
12. Parsons, M. F. *et al. Phys. Rev. Lett.* **114,** 213002 (2015).

QUANTUM OPTICS

Jumping to hyperentanglement

A state-of-the-art source of hyperentangled photon pairs has been built and its quantum properties fully characterized.

Olivier Pfister

Once considered a central oddity of quantum mechanics and the key to its incompleteness[1], entanglement is also the essential ingredient of quantum information. The most powerful quantum computing algorithms require entanglement between a large number of qubits, which can be implemented using optical modes. Furthermore, the generation of high-quality entanglement between two modes (bipartite) is still a key enabler of quantum technologies such as quantum cryptography, quantum teleportation and repeating, and quantum secret sharing.

Writing in *Nature Photonics*, Zhenda Xie and colleagues[2] demonstrate a significant experimental advance in the generation and verification of photonic bipartite hyperentangled states. Hyperentanglement[3] is the achievement of simultaneous entanglement that spans more than one degree of freedom, for example photon number, frequency and polarization (Box 1). It is an important resource for quantum information as its quantum (entangled) redundancy allows more flexibility in implementing essential Bell-state measurements as well as providing error-correction encoding features.

For their hyperentanglement experiment, Xie *et al.*[2] used a highly efficient type-II spontaneous parametric downconversion (SPDC) source comprising a long (1.6 cm) waveguide in a periodically poled potassium titanyl phosphate (PPKTP) crystal to produce orthogonally polarized photon pairs (Box 1). An optical cavity subsequently filtered the broadband 245 GHz frequency output to 17 discrete GHz bins, spaced by the free spectral range of the filter

Box 1 | Principles of hyperentanglement.

Bipartite hyperentanglement can be illustrated and obtained as follows. First, consider a perfectly entangled state of light created by two-photon emission into two well-defined optical modes, 1 and 2:

$$\sum_{n=0}^{\infty} |n\rangle_1 |n\rangle_2$$

where n is the photon number. This state is actually a perfect Einstein–Podolsky–Rosen state[13], good approximations of which can be generated by stimulated parametric downconversion in an optical parametric oscillator[14]. Here, the emission will be spontaneous parametric downconversion in a nonlinear medium in which photons from a narrowband pump field of frequency ω_p are annihilated to create pairs of signal photons at frequencies ω and $\omega_p - \omega$. Because such emitters usually have rather broad bandwidths, there can be a wide distribution of the signal photon frequency, yielding (still paying no heed to realistic normalization)

$$\int d\omega \sum_{n=0}^{\infty} |\omega; n\rangle_1 |\omega_p - \omega; n\rangle_2$$

This state is entangled both in the photon number and frequency, or hyperentangled. We can up the ante by adding polarization entanglement to the mix:

$$\sum_{\varepsilon\in\{H,V\}} \int d\omega \sum_{n=0}^{\infty} |\varepsilon, \omega; n\rangle_1 | \varepsilon_\perp, \omega_p - \omega; n\rangle_2$$

and so on, where ε is the polarization direction along the horizontal (H) or vertical (V) direction. In the case that interests us here, only photon pairs are emitted, which restricts the sum over n to $n = 1$:

$$\sum_{\varepsilon\in\{H,V\}} \int d\omega |\varepsilon, \omega; 1\rangle_1 | \varepsilon_\perp, \omega_p - \omega; 1\rangle_2$$

cavity, thereby yielding about four bits of encoding space per photon. Moreover, the temporal dependence of the transmitted light assumed a periodic, 'mode-locked' character as the filtered modes, being resonant in the filter cavity, must be temporally separated by the roundtrip time of 66 ps.

Xie *et al.* then proceeded to thoroughly characterize the source properties by making use of the well-known arsenal of quantum interference effects discovered by Hong, Ou and Mandel[4], and Franson[5].

In Hong–Ou–Mandel interference, two single, identical photons impinging separately on each input port of a balanced beamsplitter always exit together from the same output port, more precisely in a quantum superposition of both output ports. For this to happen the input photon wavepackets must, of course, arrive at the same time and overlap at the beamsplitter and any temporal delay of one with respect to the other yields the famous Hong–Ou–Mandel dip of the coincidence signal at the beamsplitter output, which provides a clear signal of the absence of the distributed photon output.

In the case of the mode-locked biphoton frequency comb used by Xie and colleagues, the Hong–Ou–Mandel quantum interference can actually happen at all time-differences equal to the pulse spacing, that is, the filter cavity roundtrip time. These 'revivals' of the Hong–Ou–Mandel dip, which could also be called recursive Hong–Ou–Mandel dips, occur as the time delay is scanned, as first predicted by Shapiro[6]. This was first observed by Ou's group[7], albeit with a less sophisticated set-up that only gave a 50%, rather than a 100%, dip depth. In the work by Xie and colleagues[2], a 96.5% Hong–Ou–Mandel dip is obtained, which constitutes the first complete observation of such recursion. In an absolute sense, a near-100% Hong–Ou–Mandel dip depth is important beyond the mere quantitative aspect because it rules out all classical explanations of the observed interference (dip).

Xie *et al.* explicitly tested the frequency correlations in the biphoton comb, which confirmed the expected symmetrical distribution with respect to the half-frequency of the SPDC pump. They then performed Franson interferometry[5], an elegant nonlocal quantum interference effect under conditions where classical coherence is lost, and thus classical interference is impossible. Franson interferometry provides a time–energy Bell inequality test, and thus a rigorous test of entanglement, as the photons are correlated in time and anticorrelated in energy. Each photon of an emitted pair is sent to a separate Mach–Zehnder interferometer whose two arms have a path difference that is much longer than the single photon coherence length. The quantum probability amplitudes for both photons taking the short interferometer arm, and for both taking the long interferometer arm, and then interfering, are measured (both long paths do not differ by more than the single photon coherence length). The interference visibility in the experiment was a very good 97.8%.

Although the observation by Xie *et al.*[2] that Franson fringes do, indeed, recur at every multiple of the roundtrip time of the filter cavity may not be very surprising, it is in fact the first observation of such an effect. The authors also observed a degradation of the fringe visibility, consistent with the theoretical expectation from the linewidth of each mode of the filter cavity.

Having convincingly established the time–frequency entangled nature of their biphoton comb, the authors proceeded to generate hyperentanglement by adding polarization entanglement. They then tested for hyperentanglement by conducting combined Bell measurements on polarization entanglement and on time–frequency entanglement, showing the violation of Bell-type Clauser–Horne–Shimony–Holt inequalities at levels near the maximum allowed by quantum mechanics.

Because they used a long nonlinear waveguide, the authors demonstrated a very high brightness for their source of hyperentangled photons, and their careful experiments demonstrated quantum interference effects with consistently high visibilities.

Where do we go from here? Xie *et al.*[2] mention that one next step could be to increase the brightness of their source by placing the waveguide inside a resonator, say, by surrounding it with Bragg mirrors. This is not yet possible because the waveguide has non-negligible levels of propagation loss (typically of the order of 0.1 dB cm^{-1}) and so further work on low-loss integrated nonlinear optics is therefore very worthwhile.

Another possibility would be to improve the system detection efficiency, which is of the order of 1% in this work. Because coincidence detection is used, the final results are post-selected and the adverse effects of this low detection efficiency, as well as of phase-mismatched SPDC emission background[8] and losses in the PPKTP waveguide, can be completely circumvented at the expense of a reduced probability of success for the coincidence measurement. This powerful redeeming method has been, justifiably, a workhorse of numerous (though not all) photonic implementations of quantum information. However, the approach hinders scalability exponentially, and scalability will be important in practical applications, as one would reasonably expect to have to resort to a multitude of quantum repeater stages, which use entangled channels, to reliably send quantum information across large distances.

Another consequence of the current coincidence set-up, besides decreasing the information flux, is to limit quantum processing to single-photon states. Overcoming these limitations with high-efficiency photon-number-resolved detection techniques[9] will allow one to address the Fock basis in earnest, giving access to more general protocols, such as quantum state tomography by photon counting[10,11] and the generation of non-Gaussian states of light[12]. ❐

Olivier Pfister is in the Department of Physics at the University of Virginia, 382 McCormick Road, Charlottesville, Virginia 22904-4714, USA.
e-mail: opfister@virginia.edu

References

1. Einstein, A., Podolsky, B. & Rosen, N. *Phys. Rev.* **47,** 777 (1935).
2. Xie, Z. *et al. Nature Photon.* **9,** 536–542 (2015).
3. Kwiat, P. G. *J. Mod. Opt.* **44,** 2173–2184 (1997).
4. Hong, C. K., Ou, Z. Y. & Mandel, L. *Phys. Rev. Lett.* **59,** 2044 (1987).
5. Franson, J. D. *Phys. Rev. Lett.* **62,** 2205 (1989).
6. Shapiro, J. H. in *Technical Digest of Topical Conference on Nonlinear Optics* (ed. Sawchuk, A.) FC7 (Optical Society of America, 2002).
7. Lu, Y. J., Campbell, R. L. & Ou, Z. Y. *Phys. Rev. Lett.* **91,** 163602 (2003).
8. Kleinman, D. A. *Phys. Rev.* **174,** 1027 (1968).
9. Calkins, B. *et al. Opt. Express* **21,** 22657–22670 (2013).
10. Wallentowitz, S. & Vogel, W. *Phys. Rev. A* **53,** 4528 (1996).
11. Banaszek, K. & Wódkiewicz, K. *Phys. Rev. Lett.* **76,** 4344 (1996).
12. Ourjoumtsev, A., Tualle-Brouri, R., Laurat, J. & Grangier, P. *Science* **312,** 83–86 (2006).
13. van Enk, S. J. *Phys. Rev. A* **60,** 5095 (1999).
14. Ou, Z. Y., Pereira, S. F., Kimble, H. J. & Peng, K. C. *Phys. Rev. Lett.* **68,** 3663 (1992).

NANOPHOTONICS

Liquid quantum photonics

Researchers have observed light propagation in which photons glide smoothly along a one-dimensional chain of electrons known as a Luttinger liquid — a many-body interacting quantum system held within a single-walled carbon nanotube.

Mark Tame

Most materials that guide light are simply described by the Lorentz model — a classical theory introduced by Hendrik Lorentz at the turn of the twentieth century. In this model, electrons are bound to atoms and form a dipole that responds to light by producing its own light field[1]. The combined fields of all the atoms in the material and that of the incoming light constitute the total field as it is guided along. The Lorentz model has played a pivotal role in the advancement of optical science in the decades since being introduced.

With rapid progress currently being made in nanofabrication, researchers are now trying to understand how to control and guide light at the nanoscale. New kinds of materials have been explored to realize compact integrated optical circuitry that can bypass the so-called diffraction limit — a limit that forbids the confinement of light to dimensions significantly smaller than its wavelength. A breakthrough came in 1997 when Junichi Takahara and colleagues[2] showed that metals are able to confine light to scales well below the diffraction limit. At an interface of a metal with a dielectric medium the light can be guided in the form of a surface plasmon polariton — a joint state of a photon coupled to an electron charge density wave. This discovery and impressive advances in metal nanostructure fabrication have resulted in intense interest in plasmonic systems from researchers keen to build high-speed optical devices for controlling light at the same scale as conventional electronics[3].

In plasmonics, the Lorentz model is superseded by the widely used Drude–Lorentz model[4], where the outer electrons of atoms are no longer bound, and move freely through the metal allowing it to conduct. This is again a classical model where the electrons are treated as a non-interacting gas with Maxwell–Boltzmann statistics. To model the electrons quantum mechanically, one should take into account their fermionic nature, in particular, the Pauli exclusion principle. To do this, the Drude–Sommerfeld model[4] can be used, where the electrons are treated as a non-interacting Fermi gas with Fermi–Dirac statistics. However, one of the main drawbacks of this description is that electron–electron interactions are not included, and these can have a big impact on the behaviour of the metal when guiding light.

To correctly model quantum electron behaviour in metals, Fermi–Landau liquid theory is needed[4]. A problem arises, though, when the electrons are confined to metallic structures that are narrow relative to their wavelength. In this case, the interacting electron system reduces to a one-dimension system and Fermi–Landau liquid theory completely breaks down. To correctly explain this one-dimensional system a Luttinger liquid model — a fully quantum mechanical theory — is required[5]. One of the hallmarks of this unusual many-body electron system is spin–charge separation, where spin waves and charge density waves propagate independently. The formation of charge density waves, or plasmons, in a Luttinger liquid is fundamentally quantum mechanical in origin, due to treating the electrons as a many-body interacting quantum system. The unique properties of Luttinger liquids have recently been observed in several impressive experiments[5], most notably in carbon nanotubes. However, there has not been any direct observation of Luttinger liquid plasmons in these systems, or their coupling to light as surface plasmon polaritons. This has been an outstanding challenge for well over a decade.

Writing in *Nature Photonics*, Zhiwen Shi *et al.*[6] now report the first observation of Luttinger liquid plasmons using metallic single-walled carbon nanotubes. Using near-field infrared nanoscopy, they show that the Luttinger liquid plasmons in a one-dimensional system behave qualitatively different from plasmons in two or three-dimensions, with 'quantized' velocities and coupling with light to form a new type of low-loss broadband optical mode that has extraordinary field confinement.

The plasmon optical mode in the Luttinger liquid is very different to previously studied plasmons in carbon nanotubes, which are simply considered to be rolled up sheets of graphene with the Drude–Lorentz model employed[7]. In the work by Shi and colleagues[6], the optical modes of the Luttinger liquid plasmons are based on a careful treatment of many-body quantum interactions between the electrons in one-dimension[8]. The work opens up new possibilities for designing some rather exotic nanoscale photonic waveguides based on interacting electronic systems. Whereas Shi *et al.*[6] have probed their metallic carbon nanotubes in the infrared, Luttinger liquid plasmons are expected to persist to visible